Title

Investigating local environment effects on the photonic interactions of cesium lead halide perovskite nanocrystals

ISBN

9798277438350

Author

Grishchenko, Alexandra Yvette

Publication Date

2026-03-12

Peer reviewed|Thesis/dissertation

UNIVERSITY OF CALIFORNIA

Los Angeles

Investigating local environment effects on the photonic interactions of cesium lead halide perovskite nanocrystals

A thesis submitted in partial satisfaction of the

requirements for the degree Master of Science in Chemical Engineering

by

Alexandra Yvette Grishchenko

2026

ABSTRACT OF THE THESIS

Investigating local environment effects on the photonic interactions

of cesium lead halide perovskite nanocrystals

by

Alexandra Yvette Grishchenko

Master of Science in Chemical Engineering

University of California, Los Angeles, 2026

Professor Carissa N. Eisler, Chair

Precise control over light emission at the nanoscale is essential for advancing energy-efficient optoelectronic devices and emerging quantum photonic technologies. As semiconductor nanocrystals approach near unity photoluminescence quantum yield (PLQY), further performance improvements depend increasingly on directing emitted photons. Lead halide perovskite ($CsPbX_3$ (X=halide)) (LHP) nanocrystals have unusually tunable angular emission due to their soft ionic lattice, which along with near-unity PLQY, defect tolerance, and facile emission wavelength tunability makes isolated LHP nanocrystals great candidates for photon qubit sources and close-packed films useful for light emitting diodes and solar energy technology. In this work, we

investigate how the interplay of nanocrystal synthesis, surface chemistry, thin film assembly, and substrate interactions collectively govern transition dipole moment (TDM) orientation and thus angular light emission in $CsPbBr_3$ nanocrystals.

We developed size- and shape-controlled synthetic protocols under ambient conditions spanning strongly quantum-confined to unconfined (3.5 - 10 nm) regimes. Optimized purification strategies were critical for preserving colloidal stability and preventing aggregation-induced spectral shifts. By comparing ligand chemistries including oleic acid/oleylamine (OA/OAm), didodecyldimethylammonium bromide (DDAB), and zwitterionic lecithin, we balanced passivation, stability, and compatibility with ordered self-assembly.

Using controlled deposition methods, we fabricated films with high density and coverage (>50%) of varied nanocrystal dimensions and oriented nanoplate assemblies. Angular emission was imaged via back focal plane fluorescence microscopy (BFPFM) and fit to an effective TDM angle using a three-layer model. Isotropic nanocrystal thin films exhibited nearly identical effective TDM angles (~40–41°) across size regimes, indicating that interparticle interactions in dense films dominate over size-mediated substrate effects. Anisotropic nanoplates demonstrated substantial tunability, with effective TDM angles varying from ~28° in face-down assemblies to ~46° in edge-up configurations.

This work demonstrates that the angular emission of lead halide perovskite nanocrystals is a tunable property governed by nanocrystal synthesis, surface chemistry, packing motif, and substrate interaction. By integrating colloidal materials synthesis and film deposition with quantitative optical modeling, we establish a design framework for engineering transition dipole alignment and directional emission in next-generation optoelectronic and quantum photonic devices.

The thesis of Alexandra Yvette Grishchenko is approved.

Jane P. Chang

Philippe Sautet

Carissa N. Eisler, Committee Chair

University of California, Los Angeles

2026

Table of Contents

List of figures

1. INTRODUCTION

At the core of our lives in the information age is an ever-growing demand for energy and computational power that enables the technology that has become ubiquitous in our everyday routine. New material and device architecture discoveries are necessary to both increase the energy efficiency of devices and achieve high-performance computing goals. A primary focus of study in energy efficiency research has been on effective electron to photon conversion, but with the recent development of emitters with near unity quantum yields, optimized photon management by controlled light emission directionality has become crucial; by approaching the problem at the nanoscale, we can surpass efficiencies traditionally limited by refractive index in bulk materials. Separately, in the fields of computation, communication, and sensing, a second quantum revolution requires sources of particles that produce qubits which are scalable, have long coherence times, and enable high fidelity measurements—identifying a reliable single photon source would transform quantum computing.[1] Finding materials that satisfy these goals of maximizing energy efficiency and advancing quantum information technologies is of great importance for next generation optoelectronic devices.

1.1 Semiconductor nanocrystals

Generally, colloidal semiconductor nanocrystals are crystalline particles 1 to 100 nm in size and can be synthesized with a wide range of sizes, shapes, and compositions to tune their optical and electronic properties. Quantum dots, which are semiconductor nanocrystals that have dimensions below the material's Bohr Radius, exhibit quantum confinement effects that result in exceptional luminescence.[2] The discovery of quantum dots, awarded the Nobel Prize in 2023, brought about ground-breaking knowledge of these quantum confinement effects and emitted light

wavelength tunability along with the potential to revolutionize optoelectronics. These particles are now widely applied in many fields including but not limited to optoelectronics (LEDs, waveguides, lasers), sensing, and medicine.[3–6]

In 2015, Protesescu et al. synthesized colloidal semiconductor nanocrystals composed of lead halide perovskites by a hot injection method under inert, heated conditions.[7] These halide perovskite nanocrystals represented a deviation from the development of increasingly covalent and structurally rigid nanocrystals (III-V and metal boride nanocrystals) due to their unusually ionic lattice and structural softness.[8–11] Lead halide perovskites adopt an ABX_3 structure, where the cation "B" is coordinated to six halides (X) in an octahedral manner and the monovalent cation "A" occupies the octahedral cavity of eight BX_6 octahedral groups. The labile lattice permits the BX_6 octahedra to tilt, often forming a distorted form of the ideal cubic lattice and allowing large organic cations in the A site. Specifically, inorganic lead halide perovskites of the form $CsPbX_3$ (X = halide) have been a focus of study for their high quantum yields, facile low-temperature ambient synthesis enabled by weak bonds, promise as coherent single photon sources for QIT, and unique collective properties like superfluorescence.[1,2,12] Figure 1.1 shows the composition-based color tunability of cesium lead halide nanocrystals achieved by Protesescu et al., and it depicts the $CsPbBr_3$ structure as well as tilted BX_6 structures. Halide perovskite nanocrystals have been synthesized using new techniques with varying compositions including A = Cs^+, methylammonium (MA^+), formamidinium (FA^+); B = $Pb2^+$, $Sn2^+$; X = Cl^-, Br^-, I^-, as well as different morphologies such as nanoplates, nanowires, and nanocubes.[2,13,14]

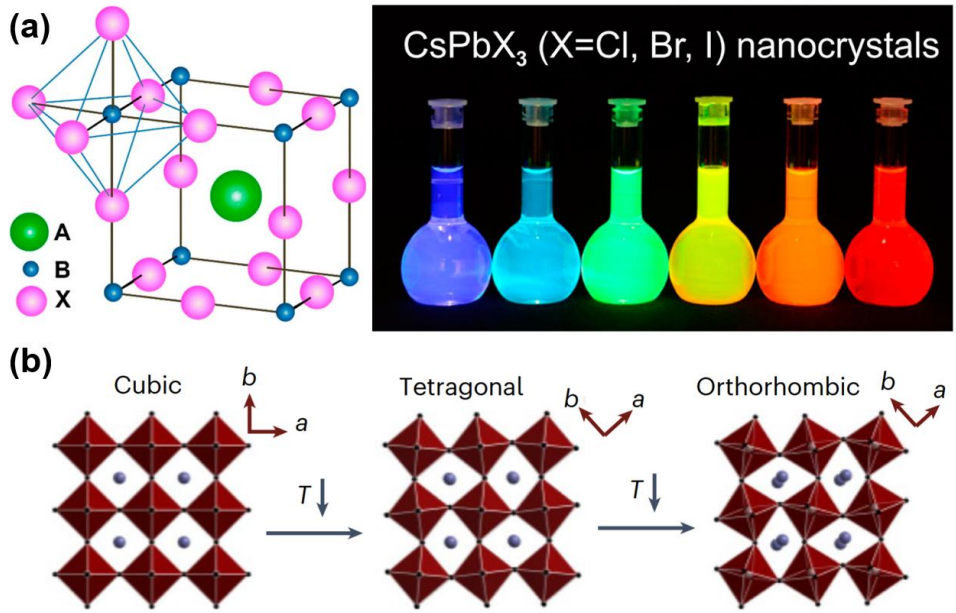

Figure 1.1. (a) Cubic $CsPbBr_3$ structure and color tunability of colloidal $CsPbX_3$ nanocrystals from Sharif et al.[15] and Protesescu et al.[7] (b) tilting of perovskite BX_6 octahedra results in formation of modified lattice structures from Zhu et al.[1]

In the decade since this discovery, these nanocrystals have already entered the commercial space as a colloidal product sold by major vendors such as Sigma Aldrich and have shown promise in applications from lasers[3] to LEDs,[4,16] photodetectors,[17] scintillators,[18] security tags,[6] luminescent solar concentrators,[5] solar cells,[19] and photonic quantum technologies.[1] Like other semiconductor nanocrystals, halide perovskites have a wide range of applications due to their composition, size, and shape tunability which allows for modulation of emission wavelength.[20,21] However, some unique properties make these nanocrystals desirable over traditional semiconductors. Recent studies have developed effective, accessible, and scalable synthetic protocols under ambient conditions,[20,22] while maintaining near-unity PLQYs[23] at emission wavelengths tunable across the whole visible spectrum.[21] Halide perovskites also exhibit

extremely rapid radiative decay that leads to their unusually bright emission,[24] as well as exceptional physical defect tolerance due to the close energetic proximity of the Pb (6p) atomic orbital to the conduction band edge.[25] Figure 1.2 summarizes achievable wavelengths by both composition and size tuning, demonstrates the band alignment that leads to exceptional defect tolerance, and depicts various TEM images of different lead halide perovskite nanocrystal shapes and sizes.

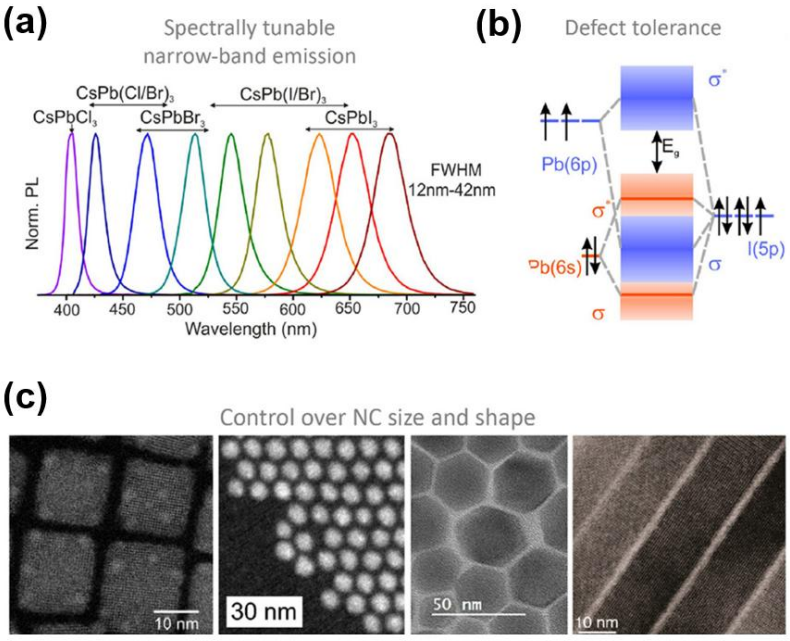

Figure 1.2. (a) Narrow-band PL is achieved across the entire visible range, with spectral tunability possible by compositional and size/shape control (b) High PLQY is attributed to defect tolerance emerging from the Pb-halide bond. (c) Size and shape control achieved of lead halide perovskite nanocrystals. From Ibáñez et al.[2]

Additionally, all these notable optical properties have been achieved with simple surface passivation by long chain organic molecules, rather than an epitaxial inorganic shell. Previously

studied II–VI, IV–VI, or III–V semiconductor nanocrystals typically require laborious core/shell synthesis processes to achieve similarly high PLQYs and passivate surface trap states that appear within the bandgap (i.e. ZnS shelled CdSe nanocrystals).[26,27] Here, due to halide perovskite nanocrystals' unique electronic structure, ligand molecules are sufficient to anchor to the ionic core, fill surface vacancies, and also prevent degradation of the soft ionic lattice by exposure to ambient conditions (moisture, oxygen).[28,29] Ligand engineering for optimal optical properties remains a challenge, as ligands used in the nascent years of halide perovskite nanocrystal research such as the oleic acid/oleylamine (OA/OAm) pair bind dynamically to the surface and compromise the stability of the particles over time. Promising new candidates include quaternary ammonium ligands such as didodecyldimethylammonium bromide, phosphonates, and zwitterionic ligands such as sulfobetaines and soy lecithin—these ligands are characterized by permanently charged groups that can bind firmly to either the A or X site vacancies on the nanocrystal surface.[30–33]

1.2 Directional light emission and device efficiency

The efficiency of optoelectronic devices depends on the effective orientation of the luminophore's photoluminescent transitions as this determines the resulting angular light emission distribution. As photons are generated through radiative recombination, electrons relax from higher to lower energy states and generate a dipole moment that leads to an anisotropic electric field and thus an anisotropic light emission pattern; light emission is inherently a directional process. The electric field formed is normal to the vector of this transition, and dictates the light emission—this vector representing the transition is referred to as the transition dipole moment (TDM).[34,35] To optimize energy efficiency and maximize light emission into desired modes, it is necessary to characterize and control effective film dipole alignment. This is quantified either as

the effective transition dipole moment (TDM) angle, the average angle between vertical and horizontal transitions and the substrate (Figure 1.3 (a)), or as the orientation factor (Θ),[36,37] the ratio of horizontal transitions to total transitions in film in similar works. In photovoltaics, the maximum efficiency is determined by the angular spread of light emission from the radiative recombination of the semiconductor.[38] In displays, the TDM angle determines how much light is emitted outward and defines the external quantum efficiency (EQE), as light emitted into angles that are trapped within the device is lost.[39] Therefore, a smaller TDM angle, or larger orientation factor, is desirable for light outcoupling. Figure 13 (b) shows how EQE changes as a function of orientation factor for OLEDs, demonstrating significant gains (>5%) in efficiency when moving from isotropic to aligned materials.

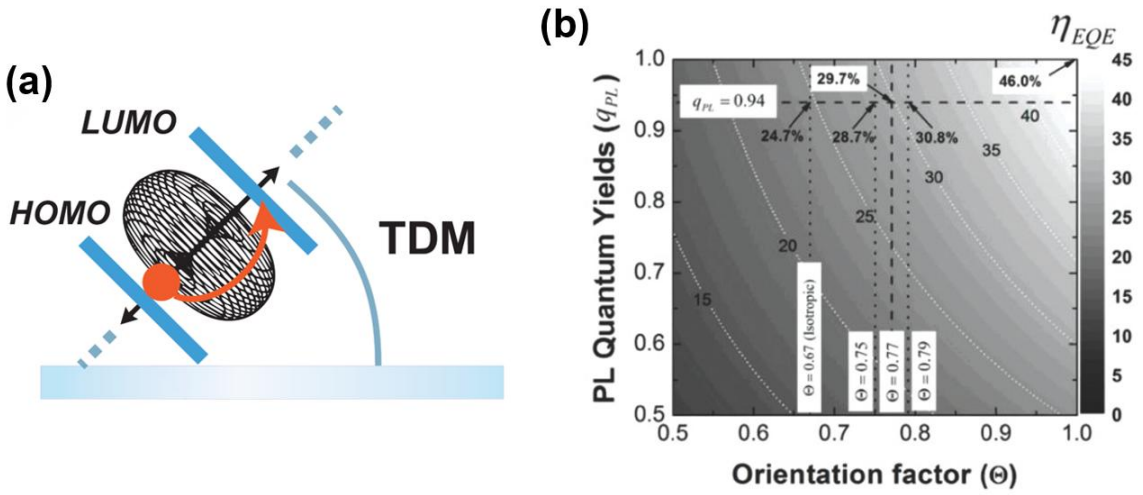

Figure 1.3. (a) The transition dipole moment angle is formed between the substrate and the vector of electronic transition. (b) External quantum efficiency (EQE) as a function of PL quantum yields (PLQY) and orientation factor (Θ) which is related to TDM angle by $TDM = \arccos(\sqrt{\Theta})$. From Kim et al.[40]

Traditional emitters such as CdSe quantum dots emit with equal contributions from two in-plane and one out-of-plane axes when deposited in a disordered film on a substrate, resulting in a film emission effective TDM angle of 35.3°.[41] For these types of particles, confinement along one axis by changing the morphology of the nanocrystal can alter the emission by eliminating electronic transitions along one of the dipole directions.[42] Because of their isotropic shape and unconfined electronic transitions, 10 nm-sized $CsPbBr_3$ perovskite nanocubes are predicted to have isotropic dipole alignment (TDM angle = 35.3°). However, inorganic lead halide perovskite nanocrystals demonstrate interesting and unexpected optical properties when deposited on a substrate with a work function mismatch. This mismatch leads to interfacial charge redistribution and results in a unique dipole response, wherein the out-of-plane (vertical) dipole of $CsPbBr_3$ nanocrystals becomes exaggerated. Recent studies have demonstrated that this exaggeration occurs on most substrates for even isotropically shaped $CsPbBr_3$ nanocrystals, resulting in an increased effective TDM angle of 47° for dense monolayer $CsPbBr_3$ nanocube films on glass.[43–45]

This increase in TDM angle means an increase in light emission parallel to the substrate, useful for applications like luminescent solar concentrators (LSCs) where light needs to be guided towards the edges of the substrate. Traditional semiconductor nanocrystals such as CdSe quantum dots do not demonstrate the same facile yet effective tunability, and require precise nanocrystal shape and ordered assembly control to achieve similar results.[42] Generally, changing the TDM angle and thus the resulting angular emission distribution can mean significant improvements in optoelectronic device efficiency; using an emitter with an effective TDM angle 8° lower than an isotropic emitter (35° to 27°) would result in an external quantum efficiency increase of 24.7% for an OLED device.[40] $CsPbBr_3$ films of different morphologies and packing densities have demonstrated a wide range of effective TDM angles from 29° for nanoplates on glass to nearly 60°

for sparse nanocubes on glass.[43,44] By exploring the extent of tunability of the effective TDM angle of $CsPbBr_3$ nanocrystal thin films, we can modulate angular emission and develop a library of techniques to optimize optoelectronic device efficiency.

Guided by results from prior literature, we aim to extract dipole alignment information from $CsPbBr_3$ films ranging from single component to multicomponent;[46,47] assembled in an ordered or disordered manner; and with nanocrystal sizes in strongly and weakly quantumly confined regimes.[20,48] To characterize the angular emission pattern of these films, we use Back Focal Plane Fluorescence Microscopy (BFPFM), also known as Fourier plane imaging, where the image of the emitted light is deteriorated by a Bertrand lens.[42,49,50] The 3D angular emission signal is projected into a 2D plane by changing the microscope focus from the sample plane to the Back Focal Plane.[50,51] By fitting this image to a model generated image by chi^2 minimization, we can extract the effective TDM angle of the film to obtain information about the ratio of contribution from out-of-plane to in-plane dipoles. The model generates a predicted angular emission pattern for a particular sample based on a three-layer simulation of the substrate, emitting layer, and air above. For this technique, a close-packed monolayer sample with long-range homogenous ordering is ideal, requiring careful tuning of the thin film assembly steps.[42]

1.3 Thesis overview

The light emission of lead halide perovskite nanocrystals is sensitive to their local environment, as demonstrated by the exaggeration of their vertical dipole on most substrates. In this work, I investigated the impact that the local environment of $CsPbBr_3$ nanocrystals has on their emission. I varied whether the films are ordered or disordered, single component or multicomponent, and composed of quantumly confined or unconfined nanocrystals. I synthesized

$CsPbBr_3$ perovskite nanocrystals that have both isotropic and anisotropic morphologies using both in-air and air-free techniques, and I achieved size-uniform isotropic nanocrystals with size tunability from 3.5 to 11 nm under ambient conditions, characterized by Transmission Electron Microscopy (TEM). The nanocrystals are capped with organic ligands that represent three generations of nanocrystal surface chemistry studies including oleic acid/oleylamine (OA/OAm), didodecyldimethylammonium bromide (DDAB), and soy lecithin. I deposited these nanocrystals on glass substrates by spin coating or liquid-air interfacial assembly and characterized the uniformity and thickness of these films using Atomic Force Microscopy (AFM). I successfully achieved monolayer DDAB-capped nanocrystal surface coverages of >90% by functionalizing the glass surface using silanization and optimized deposition techniques. The effective Transition Dipole Moment (TDM) angle of dense films is characterized by BFPFM. For isotropic particles, the effective TDM angle of both single-component and binary strongly quantumly confined and unconfined $CsPbBr_3$ nanocrystal films are shown to be nearly identical at 40±5°, likely closer to isotropic TDM angle than literature values due to aggregation of OA/OAm-capped particles, which will be mitigated in future studies. For anisotropic particles, $CsPbBr_3$ nanoplates assembled face down have an effective TDM angle of 28±2° while edge up yields 46±2°. Figure 1.4 summarizes this work.

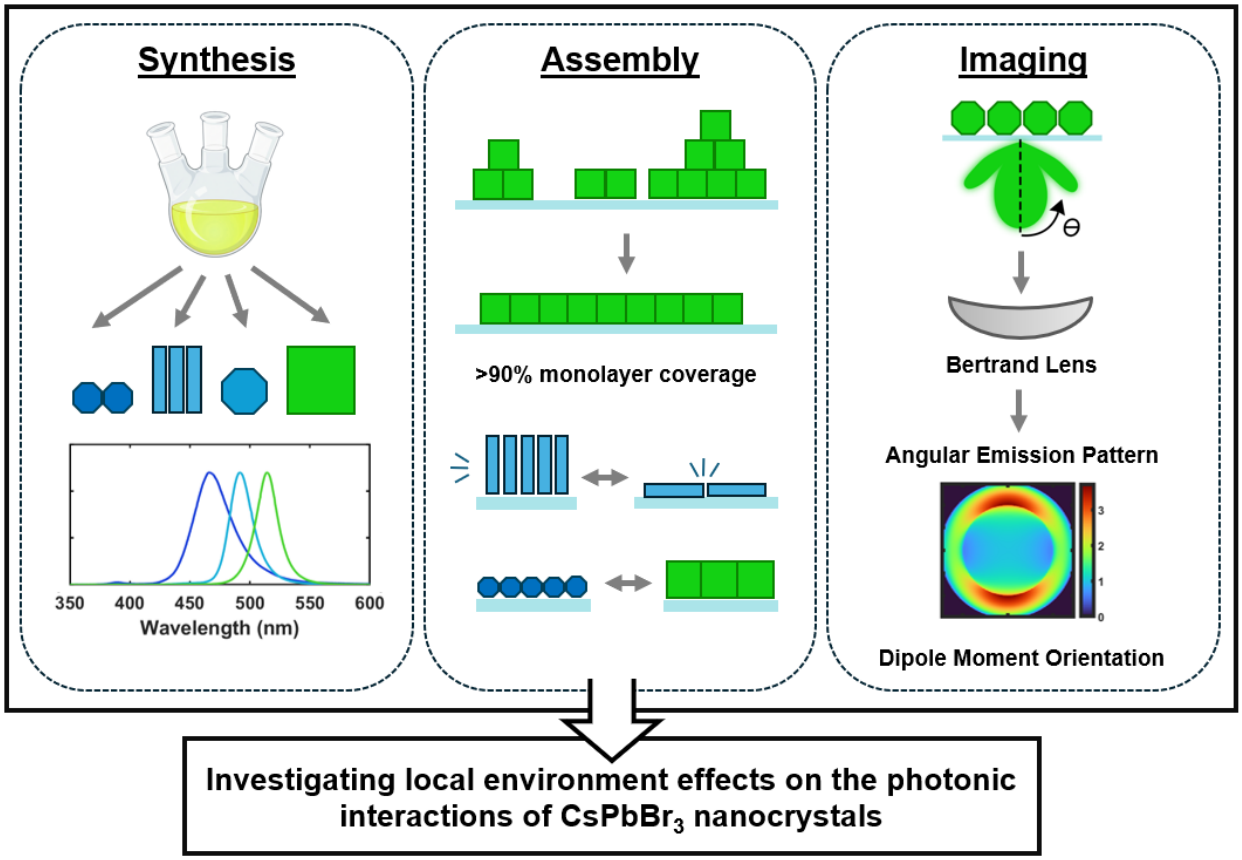

Figure 1.4. Summary of the following three chapters of thesis work: $CsPbBr_3$ nanocrystal synthesis, assembly into thin films, and optical characterization of film emission for extraction of effective TDM angle.

2. SIZE-TUNABLE SYNTHESIS OF COLLOIDAL PEROVSKITE NANOCRYSTALS

To fabricate lead halide perovskite nanocrystal thin films with various packing motifs, degrees of quantum confinement, and ordered assemblies, our first step was to synthesize nanocrystals with a range of tunable properties such as size, aspect ratio, and capping ligands. To ensure close-packed self-assembly and eliminate size and shape dependent variations, our goal for each synthesis was to generate size-uniform nanocrystal cores encapsulated by a selected organic molecule ligand (Figure 2.1).[52] We iterated through three main synthetic approaches to form $CsPbBr_3$ nanocrystals: a high temperature hot injection approach for isotropic shape (cube) and anisotropic shape (i.e. nanoplate) particles based on the one first developed by Protesescu et al.[21] in 2015, and two types of room temperature ligand-mediated approaches for isotropic particles– one developed by Brown et al.[22] in 2021, and a further optimized one described by Akkerman et al.[20] in 2022. All three syntheses rely on injection of a cesium precursor into a lead solution to initiate nucleation, however the reaction pathways towards achieving the final product vary significantly.

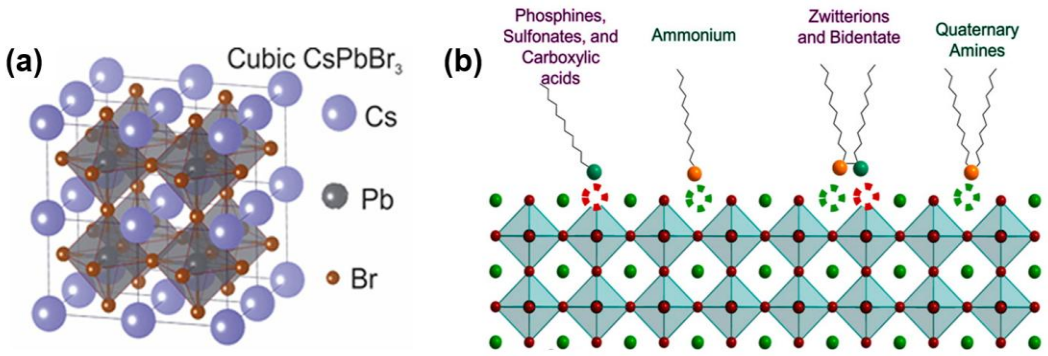

Figure 2.1. (a) $CsPbBr_3$ crystal structure from Protesescu et al.[21] (b) Nanocrystal surface termination and binding by different ligand classes from Fiuza-Maneiro et al.[30]

2.1 Protocol for $CsPbBr_3$ nanocrystal synthesis

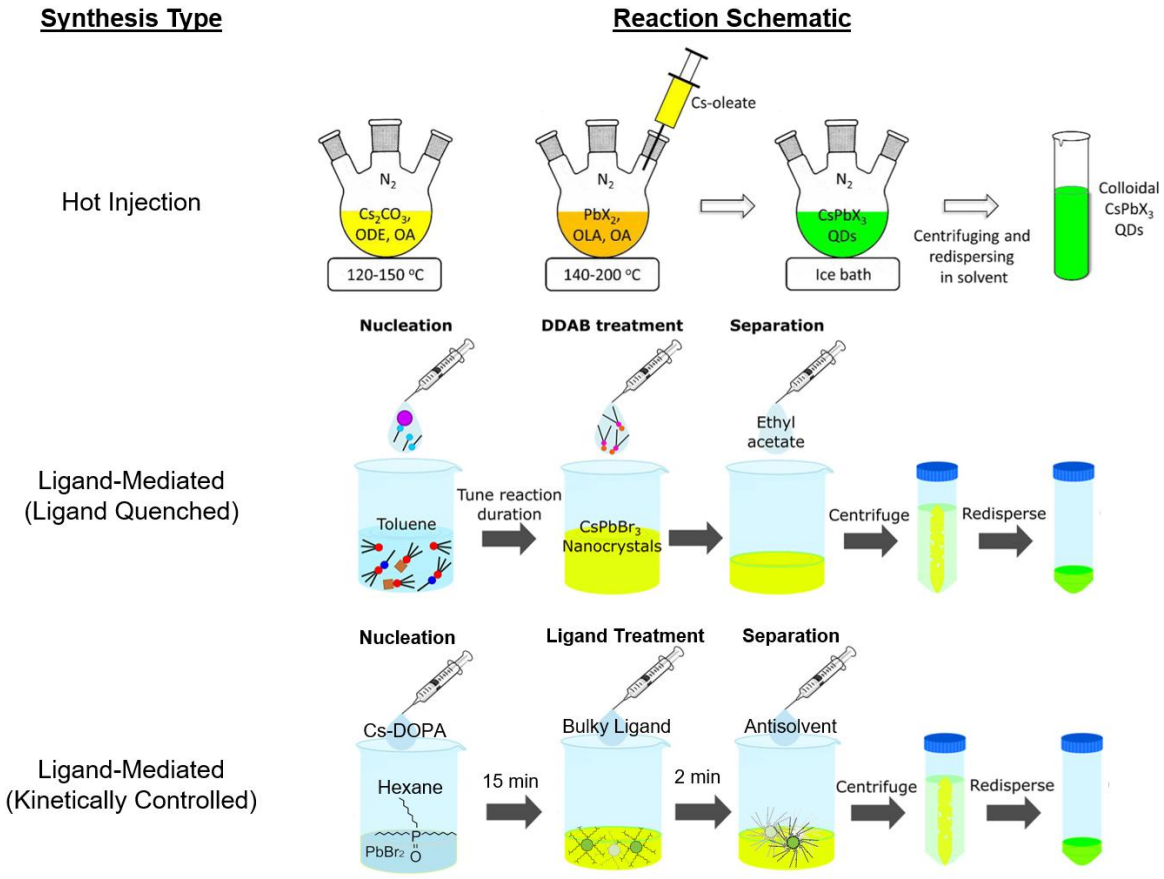

Figure 2.2. Summary of hot injection, ligand quenched, and kinetically controlled ligand mediated $CsPbBr_3$ synthesis techniques. Adapted from Chaudhary et al., Brown et al., Akkerman et al.[20,22,53]

$CsPbBr_3$ nanocrystals were synthesized by different techniques to achieve desired size and morphology. Nanoplates with an average length of 14 ± 3 nm and a thickness of 4 ± 1 nm were synthesized using a hot injection protocol adapted from Bertolotti et al.[54] Cesium carbonate was heated with oleic acid under inert conditions to form cesium oleate. Lead bromide in mesitylene was dried under vacuum at room temperature and then solubilized using oleic acid and oleylamine while being heated under inert conditions. The temperature was changed to 99 °C and cesium

oleate was injected once heated. The reaction was immediately quenched, the cyan colloidal product was cleaned, and the size was selected for further use by centrifugation.

$CsPbBr_3$ nanocrystals were synthesized by ambient ligand mediated techniques that were either ligand quenched or kinetically controlled. The ligand quenched protocol by Brown et al. permitted synthesis of particles from 6.8 to 13.6 nm in size.[22] Cesium carbonate was complexed with octanoic acid (OctAc) to form cesium octanoate. This solution was injected under ambient conditions into lead bromide solubilized with trioctylphosphine oxide (TOPO). Octylphosphinic acid (OPA) was additionally added between 0.6 and 0.1 M to tune the size of the particles between 5.8 and 13.6 nm. To terminate the reaction, a solution of a bulky didodecyldimethylammonium bromide (DDAB) ligand in toluene was introduced after five minutes. The product was cleaned by centrifugation both with and without antisolvent added.

The kinetically controlled ligand mediated synthesis protocol by Akkerman et al. allowed for synthesis of particles in a broader range of sizes from 3.5 to 10 nm.[20] A lead precursor was made by solubilizing $PbBr_2$ using TOPO in octane at 120 °C, then subsequently cooled and diluted with hexane. Into this, a cesium-diisooctylphosphinate (CS-DOPA) solution was injected, which was prepared by combining cesium carbonate with diisooctylphosphinic acid (DOPA) in octane at 120 °C and then diluted with hexane. An additional TOPO precursor which consisted of TOPO in hexane was used to further control the size of the final particles. The weakly binding intermediate ligands TOPO and DOPA were exchanged at the end of the reaction by a stronger binding ligand of choice (OA/OAm, DDAB, or zwitterionic ligands) to prevent degradation during isolation and purification. The product was cleaned by centrifuging with antisolvent.

2.2 Optimization of $CsPbBr_3$ nanocrystal synthesis for size tunability

The hot injection synthesis is performed on a Schlenk line to create an inert, heated environment. Achieving a uniform size distribution with this technique requires rapid, uniform cooling, and size tunability for isotropic particles typically ranges from 5-10 nm only.[55] We were able to instead synthesize nanocrystals under ambient conditions with precise size control using ligand-mediated techniques. The reaction developed by Brown et al. yielded size uniform nanocrystals but could not produce quantumly confined particles much smaller than the $CsPbBr_3$ Bohr diameter (~7 nm), which were of interest to us for substrate effect and energy transfer structure studies.[48] Since this synthesis relies on injection of a final ligand for reaction quenching, forming small nanocrystals is challenging due to the noncovalent and highly dynamic manner of ligand binding which makes it particularly difficult to arrest growth and stabilize small particles.[31]

The synthesis presented by Akkerman et al. allowed us to reap both the benefits of an ambient, scalable synthesis, as well as improved size tunability into the strongly quantumly confined regime with size tunability from 3.1-13 nm.[20] This synthetic pathway is characterized by successful mutual chemical equilibrium achieved between the precursor-monomer-QD nuclei conversion path permitted by a common complexing reagent, TOPO, which solubilizes the $PbBr_2$ precursor, binds to the $Cs[PbBr_3]$ monomer, and then weakly coordinates to the nucleus surface. This allows for separation of the nucleation and growth steps, like the synthesis shown by Brown et al., and it additionally imposes a self-limiting character on the reaction which achieves near 100% yield and eliminates the need for quenching by ligand injection. Due to the mutual equilibrium between different growth stages, the reaction is kinetically controlled and proceeds at a much slower rate, occurring over up to 30 minutes for larger TOPO-controlled particles. Figure 2.3 depicts approximately 10 nm $CsPbBr_3$ nanocrystals synthesized by hot injection and ligand-

mediated techniques. All 3 syntheses show similar PL peaks from 513-515 nm; variation is due to small changes in the average size and uniformity of the particles and environment (concentration of particles, solvent environment).

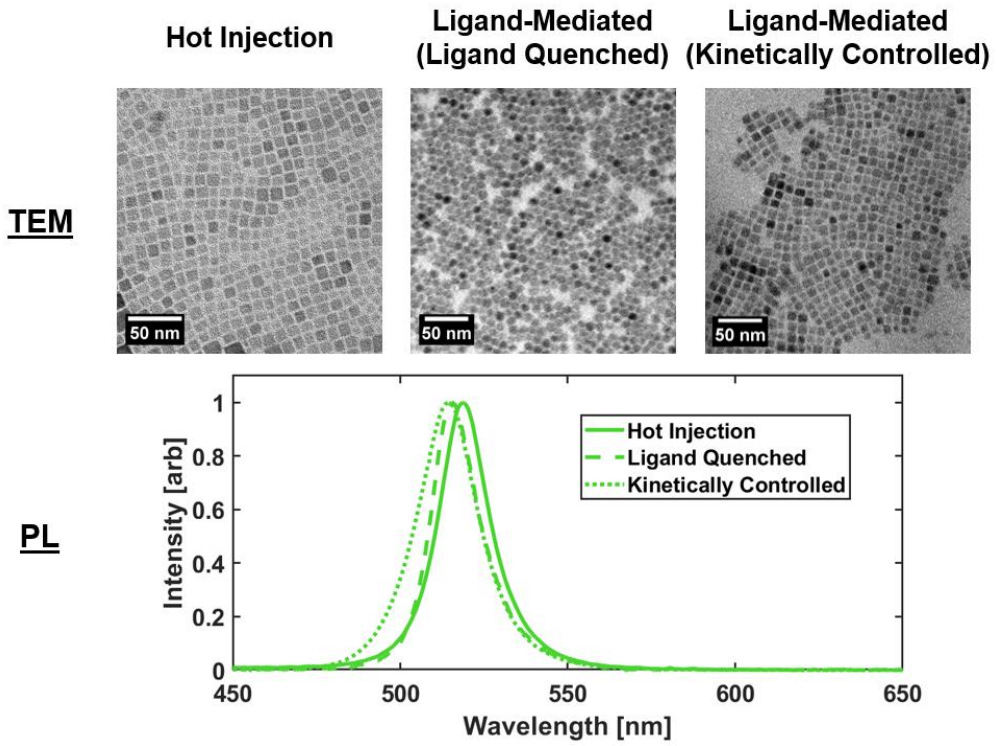

Figure 2.3. TEM and PL of synthetic products for approximately 10 nm particles from hot injection (capped with OA/OAm) and ligand mediated syntheses, both ligand quenched (capped with DDAB) and kinetically controlled (capped with OA/OAm).

Relative TOPO concentration and degree of reagent dilution effectively controlled the rate of nucleation and growth, allowing us to achieve narrow size distributions of the final particles. We faced challenges in purifying the particles, as the dilution which was necessary to achieve size control also prevented antisolvents from reducing the nanocrystal colloidal stability enough to form a pellet upon centrifugation. We discovered that even for small batches, it was necessary to

use a rotary evaporator to remove approximately 95% of the solvent and concentrate the colloid before performing antisolvent purification. Without this step, upon addition of the appropriate amount of antisolvent, there was no change in the colloidal stability of the nanocrystals as indicated by no increase in the turbidity of the solution. With a large excess of antisolvent, ligands were stripped and the nanocrystals aggregated, leading to a red-shifted emission peak wavelength. Figure 2.4 displays the PL and absorbance information for 3.5, 4.5, 5, and 10 nm OA/OAm capped particles, as well as TEM images of the 4.5, 5, and 10 nm OA/OAm capped particles. The full-width at half-maximum (FWHM) of the PL peak increases for smaller particles as anticipated from Akkerman et al.

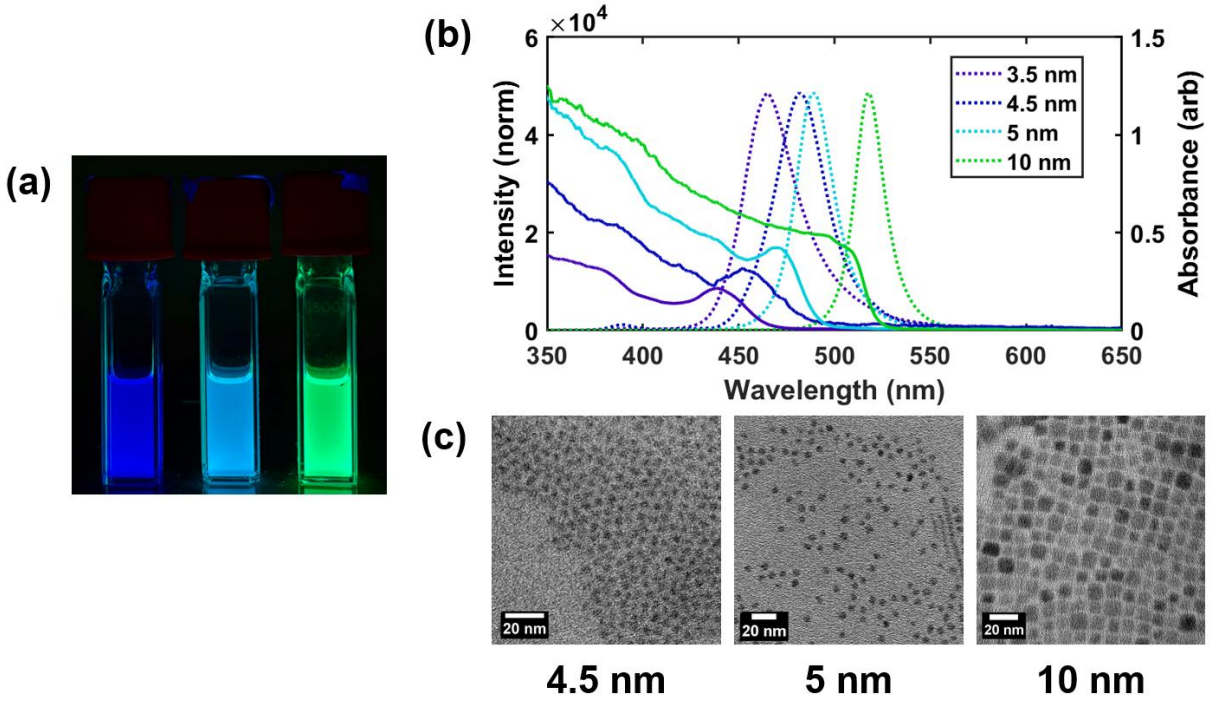

Figure 2.4. Synthetic products for kinetically controlled ligand-mediated synthesis with OA/OAm ligands; (a) Photograph of 3.5, 5, and 10 nm particle solutions with OD 1.5 at 350 nm, (b) PL/Abs for 3.5, 4.5, 5, and 10 nm particles and (c) TEM for 4.5, 5, and 10 nm particles.

2.3 $CsPbBr_3$ nanocrystal ligand selection for thin film assembly

We achieved sufficient size and shape uniformity along with size control of the $CsPbBr_3$ nanocrystal core by optimizing our synthetic protocol. Ligand choice for the final encapsulation was another key consideration to prevent degradation of the ionic core, which is sensitive to ambient moisture and oxygen. Surface ligands also define the interaction of nanocrystal with the substrate and energy transfer to other NCs, making the choice essential for studies on thin film assembly and interparticle interactions. Three generations of ligands represent advancements in the field of LHP NC synthesis: OA/OAm as the first, DDAB the second, and zwitterionic ligands such as lecithin the third.[20–22,32] Figure 2.5 demonstrates the binding sites of different ligand classes to the nanocrystal surface.

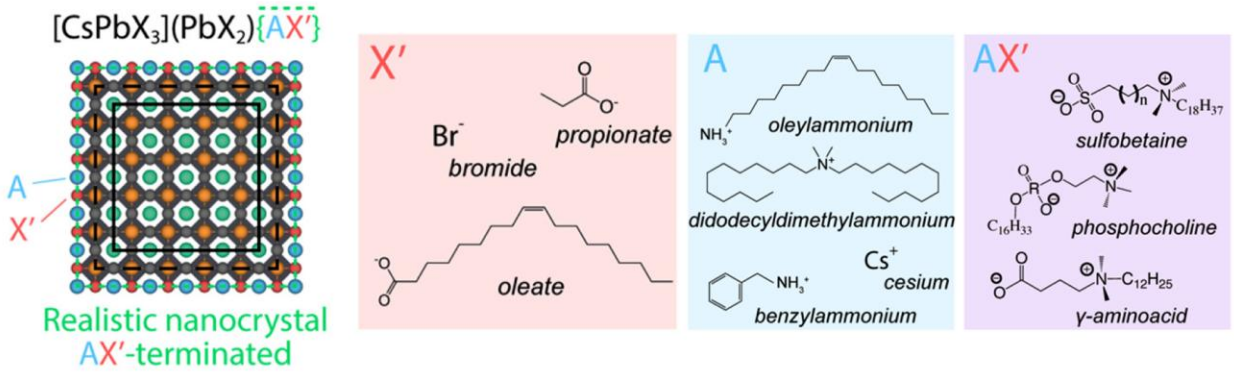

Figure 2.5. Schematic of various ligand types binding to the $CsPbBr_3$ surface. From Bodnarchuk et al.[23]

The OA/OAm ligand pair transforms into an oleate anion and oleylammonium cation, and the oleylammonium cation then substitutes up to 50% of the A cation sites.[56] The main challenge with the OAm/OA pair is its weak and dynamic surface binding, which causes the bound ligands

to be easily detached after multiple antisolvent washing steps, exposing the core to ambient moisture and oxygen and creating dangling bonds that can trap photogenerated charge pairs and quench PL.[57] In contrast, DDAB is a quaternary ammonium salt which dissociates into a permanently charged DDA^+ cation that is pH-independent and binds more strongly to the A sites, showing an improvement in stability and PLQY.[23] Additionally, an important consideration for energy transfer studies was tunability of the ligand alkyl chain length; for example, the OAm/OA pair's relatively longer chain may inhibit charge transport.[30] The newest class of zwitterionic ligands have both a positively and negatively charged group, allowing them to bind tightly to both A and X type sites. Lecithin, a zwitterionic phospholipid, allows for high colloidal stability through both tight binding to the surface and increased particle-particle repulsion due to natural polydispersity of chain length.[33] Reduced ligand desorption and increased repulsion between nanocrystals prevents aggregation, which is desirable for studies of isolated nanocrystals, but these traits interfere with large scale self-assembly techniques, where attraction between particles is necessary to form assembled films as the native solvent evaporates.

Although the Akkerman et al. synthesis used lecithin for its advantageous properties preventing aggregation during long term storage, we both adapted the synthesis to permit self-assembly and faced challenges with binding lecithin to the nanocrystal surface. The peak emission PL wavelength of lecithin treated samples red-shifted significantly upon addition of antisolvent as compared to OA/OAm ligands–this suggests that the ligand is poorly bound and adding the antisolvent induces aggregation. The synthetic product exchanged with lecithin also red-shifted significantly upon concentration with the rotary evaporator, even before the addition of antisolvent. We performed NMR on two purchased lecithin powders, one of which was identical to the product used in Park et al.[58] for the same synthesis, and confirmed that the compounds were the expected

structure despite poor synthetic results (see appendix). Ideally, DDAB would be used to functionalize the surface of the particles rather than OA/OAm as OA/OAm films suffer from aggregation, but DDAB induced etching[59] of the surface remains a project challenge as it destroys the 3.5 nm particles. Figure 2.6 summarizes these results and displays the PL before and after antisolvent addition for both unconcentrated and concentrated lecithin and OA/OAm treated samples. A turbidity change after antisolvent addition indicates that the sample can be separated by centrifugation after addition of antisolvent; the unconcentrated OA/OAm sample is stable with antisolvent addition but cannot be cleaned without concentrating on the rotary evaporator first. For future work, lecithin exchange will be optimized for single particle studies where preventing aggregation is desirable.

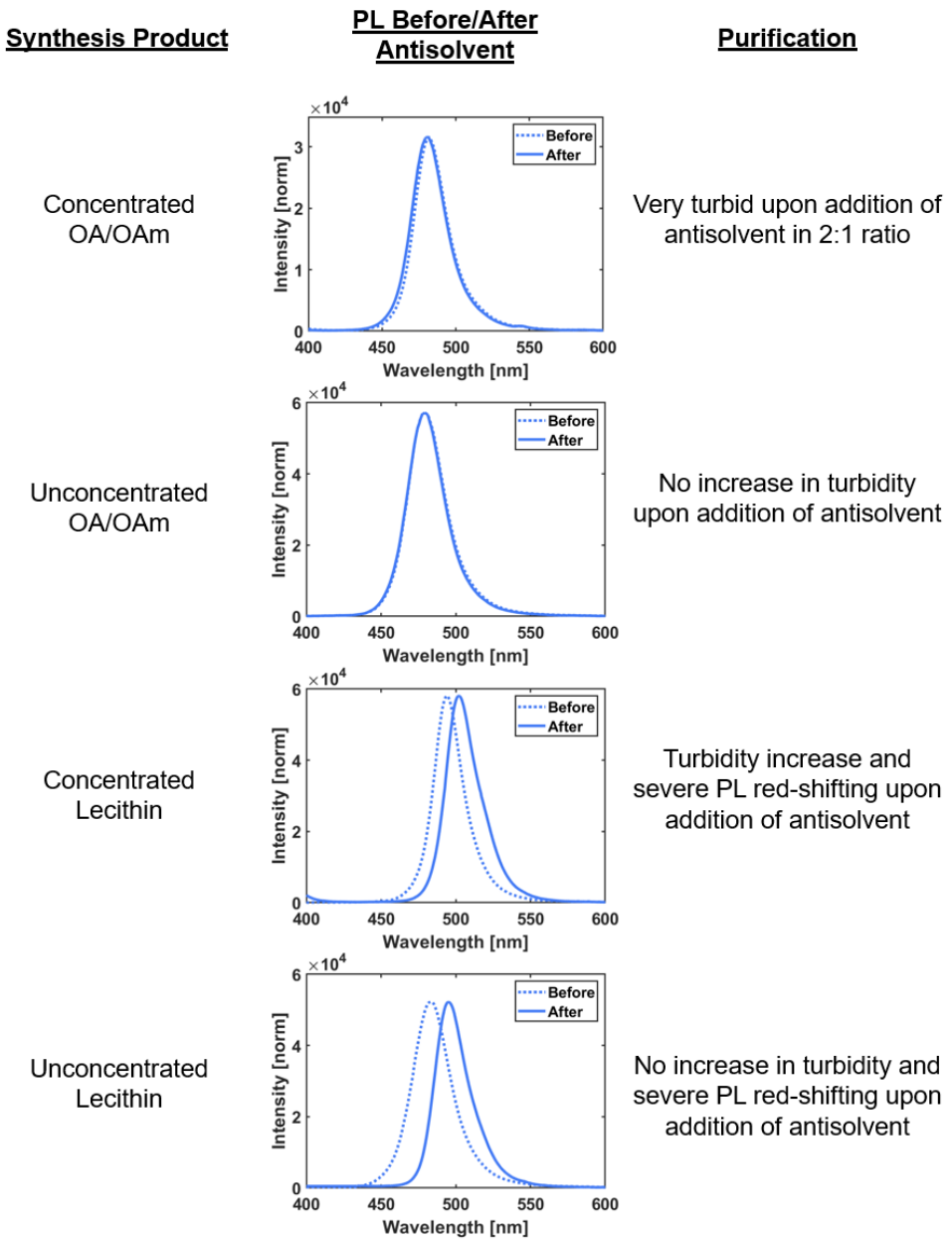

Figure 2.6. Effects of 1) ligand exchange to lecithin or OA/OAm and 2) concentration of the raw product on a rotary evaporator on the PL and turbidity of the colloidal NC solution after antisolvent addition. Turbidity increase indicates that centrifugation yielded a pellet of purified product.

2.4 Summary

To achieve successful assembly of lead halide perovskite nanocrystals into structures for angular emissions and energy transfer studies, stable and monodisperse nanocrystals are necessary. Selecting and optimizing the appropriate synthetic technique for size control capabilities, ligand properties, and effective purification is necessary for assembly and successful optical characterization. We used three synthetic approaches to generate $CsPbBr_3$ nanocrystals: anisotropic and isotropic particles generated by hot injection under inert conditions, and isotropic particles generated by ambient ligand mediated syntheses that were either ligand quenched or kinetically controlled. The ligand mediated and kinetically controlled synthesis presented by Akkerman et al. allowed us to synthesize isotropic $CsPbBr_3$ nanocrystals 3.5-10 nm in size under ambient conditions; the other syntheses could not synthesize isotropic particles that were as strongly quantumly confined. Our work shown here on nanocrystal synthesis serves as a foundation for the following chapters, which elaborate on our studies of lead halide perovskite nanocrystal's unique response to their local environment, particularly to their packing motif and nanocrystal size as a function of degree of quantum confinement.

3. FABRICATION OF PEROVSKITE NANOCRYSTAL THIN FILMS FOR INVESTIGATING LOCAL ENVIRONMENT EFFECTS

The energy transfer and light emission characteristics of lead halide perovskite nanocrystals are sensitive to their local environment, which includes both their substrate and the packing motif of neighboring particles. Rainò et al. demonstrated that assemblies of highly size-uniform 9.5 nm $CsPbBr_3$ nanocrystals with a size standard deviation of less than 5% exhibit superfluorescence, a quantum-light property in which many dipoles spontaneously align in phase to emit photons collectively with a much faster lifetime.[12,46] Superfluorescence properties are desirable for coherent laser sources and novel quantum system applications. Beyond ordered assemblies of larger particles, quantumly confined particles smaller than the $CsPbBr_3$ Bohr diameter of ~7 nm have demonstrated interesting optical properties such as non-monotonic size-dependent exciton radiative lifetime. Abbas et al. showed that while the lifetime of strongly and weakly confined nanocrystals (4.5 and 7.5 nm edge length, respectively) was long, intermediately confined nanocrystals (5 nm edge length) were found to display the shortest radiate lifetimes.[48] Anisotropic semiconductor nanocrystals have also been assembled to control their light emission properties, particularly to increase efficiency of LEDs by aligning the transition dipole moment parallel to the surface plane. Gao et al. successfully controlled long-range assembly of CdSe nanoplatelet films into face-down or edge-up orientations using liquid-air interfacial assembly and quantified angle-dependent emission by Fourier microscopy.[42] Finally, fundamental studies of emission from individual, isolated $CsPbBr_3$ nanocrystals in sparse films are of interest for quantum information technologies, where great control over production of coherent single photons with identical properties is desired.[1]

To investigate the electronic transitions leading to these properties, we studied the angular emission patterns of a variety of nanocrystal thin films that were single- or multi-component; ordered or disordered; and with nanocrystal sizes in strongly and weakly quantumly confined regimes (Figure 3.1). Previous literature indicates that changing these parameters leads to a change in the dipole orientation of the nanocrystals by modulating the relative intensity of substrate and neighboring nanocrystal effects.[42,43,45] For these studies, monolayer thickness films with both complex ordering as well as long-range uniformity (μm to mm) and high coverage (>50%) are ideal to probe substrate effects. Beyond monolayers, larger organized assemblies, such as superlattices, are also of interest to study. To achieve the control over nanocrystal assembly required for these experiments, advanced film deposition techniques are necessary to control the interplay of substrate and ligand interactions.

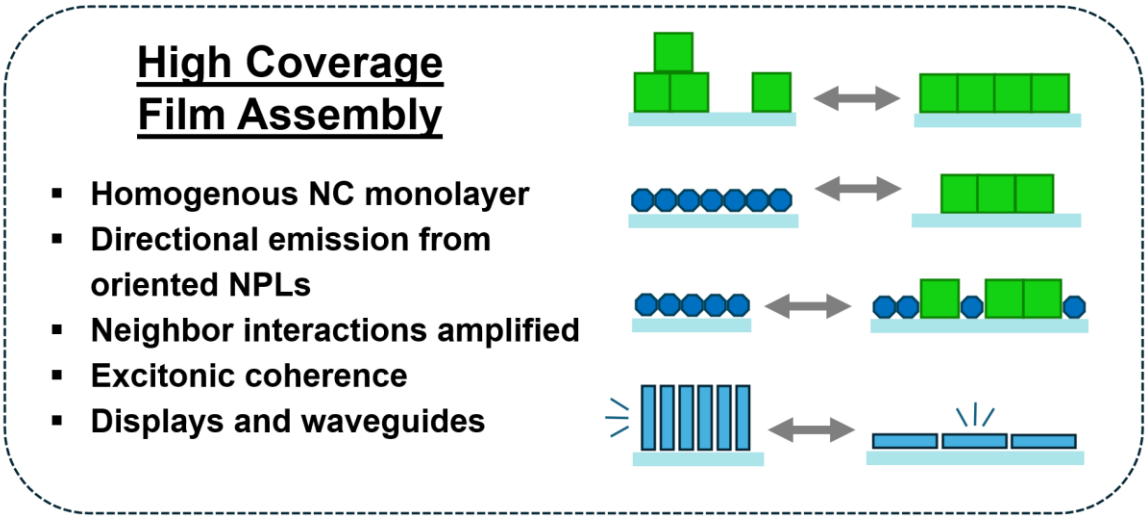

Figure 3.1. Summary of $CsPbBr_3$ high coverage (>50% substrate coverage) nanocrystal thin film assembly goals, expected photonic interactions, and applications.

3.1 Deposition of monolayer packed films of isotropic $CsPbBr_3$ nanocrystals

Uniform monolayer packed films on glass substrates are desirable for energy transfer studies and device applications, so it is imperative to pretreat the glass to improve adhesion of the nonpolar long chain ligands to the polar SiO_2 surface. Jurow et al. described the packing motif on untreated SiO_2 as large islands of aggregated nanocrystals separated by hundreds of nanometers and emphasized that changing the solution concentration had little effect on this result. Increasing the concentration of the solution does not create a densely packed film, but rather larger aggregated islands, and dilution yields islands that are further apart rather than isolated nanocrystals.[60] Strategies to functionalize the SiO_2 surface to improve adhesion include depositing polymerized hydrocarbon, polyethylenimine coating, or silanization by alkoxysilane reagents.[60–62] We used a solution based process to treat our slips whereby coverslips were first sonicated in isopropanol and acetone to remove organic contaminants, then soaked for 30 minutes in an 80 mM solution of (3-mercaptopropyl)trimethoxysilane (MPTMS) and toluene. The MPTMS methoxy groups hydrolyze to silanol groups and bind with the Si-OH glass surface to form siloxane bonds; afterwards, adjacent molecules cross-link to form the final silane layer (Figure 3.2 (a)). Miranti et al. confirmed that plasma-cleaned MPTMS treated quartz substrates demonstrated an increase of water contact angle from 7.1° to 73.9°, confirming that the polarity of the surface is modified to promote adhesion of the nonpolar organic ligand coated nanocrystal surface.[61]

We used two techniques for nanocrystal thin film deposition: spin coating and liquid-air interfacial assembly. Spin coating involves rotating the substrate at high speeds of at least 1000 rpm to introduce centripetal force that, when combined with the solution surface tension, pulls the solution into an even layer. Most of the colloidal solution is expelled from the surface as the rotation speed of the fluid and substrate equilibrates, and any remaining solvent finally evaporates

to leave behind a film. Spin coating is quick and applied easily to a variety of substrates, allowing us to create thin films with a range of nanocrystal packing density by modulating the concentration of our nanocrystal solution. We observed an improvement in nanocrystal island packing density and film uniformity when using MPTMS treated coverslips, as characterized by Atomic Force Microscopy (AFM). Figure 3.2 (b) depicts AFM data of an identical volume (75 μL) of a 40x diluted 5 mg/ml solution of DDAB-capped 10 nm $CsPbBr_3$ nanocrystal solution spin coated at 1000 rpm for 30 seconds on both an untreated and MPTMS treated coverslip. While total surface coverage by nanocrystals remains approximately the same at 32% for both untreated and treated coverslips, of the covered surface area 79% is a nanocrystal monolayer for the untreated coverslip as compared to 95% for the treated coverslip.

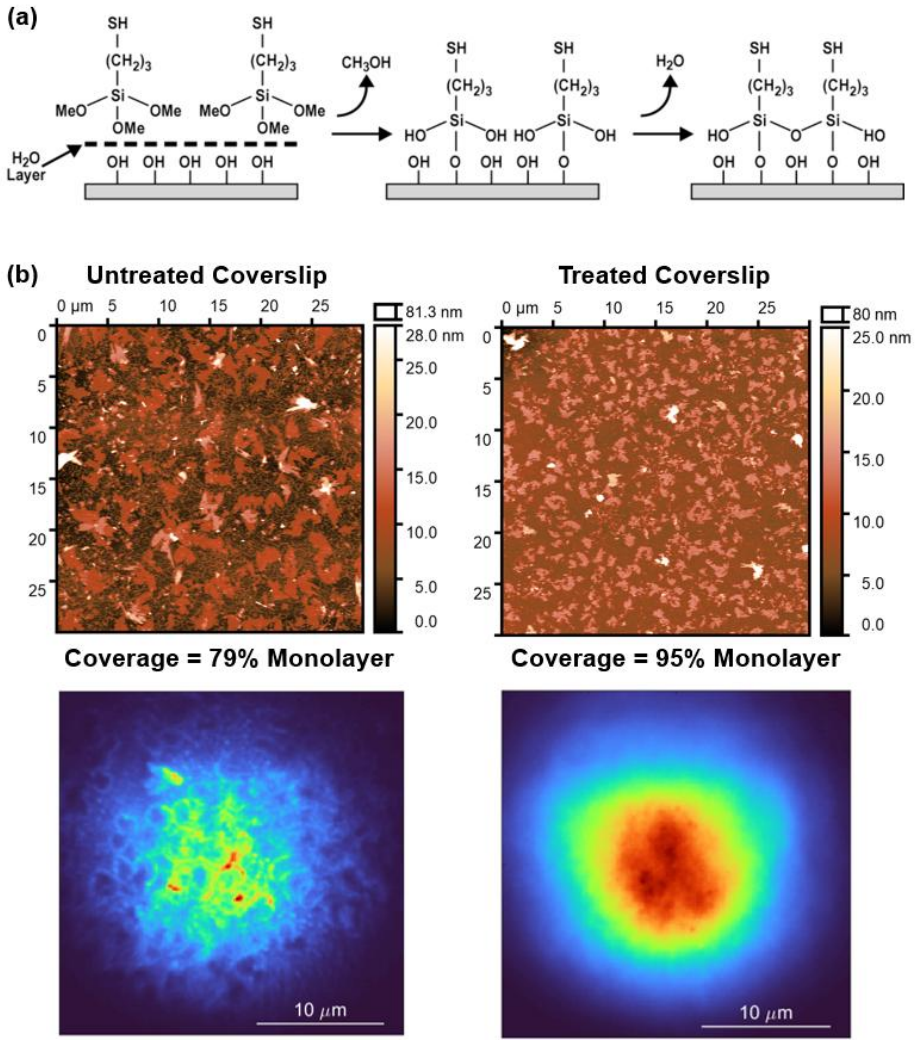

Figure 3.2. (a) Schematic of MPTMS SiO_2 silanization. Adapted from Singh et al.[63] (b) AFM and wide field PL imaging of 75 µl sample spin coated on an untreated and MPTMS treated glass coverslip.

While spin coating on treated substrates greatly increases the packing and area coverage, these films are packed in random orientations; therefore, a more advanced deposition technique is required for studies that probe the effect of highly ordered packing. Liquid-air interfacial assembly has been widely used to achieve long-range ordering of nanoparticles on the order of um to cm.[47,64,65] This method takes advantage of tuning interfacial and intermolecular forces to an energetic minimum at the desired assembly motif, either by tuning concentration of nanoparticles, introducing ligand into the sublayer, particle size, or controlling solvent evaporation rate. Liquid-air interfacial assembly has been used to control orientation of chalcogenide and CdSe nanoplatelets, and to form superlattices and binary monolayer assemblies of isotropic lead halide perovskite nanocrystals.[42,66] Figure 3.3 summarizes the liquid-air interfacial assembly protocol used for $CsPbBr_3$ studies in this work, which involves depositing a standardized volume and dilution of stock solution on an immiscible sublayer in a petri dish. Glyceryl triacetate (GTA) was selected for our immiscible sublayer as it was found to produce minimal red shifting and less PL degradation as compared to acetonitrile or diethylene glycol. The petri dish is then covered to control the rate of solvent evaporation and prevent ambient convection. The final film is transferred by stamping the substrate (treated coverslip or TEM grid) onto the surface.

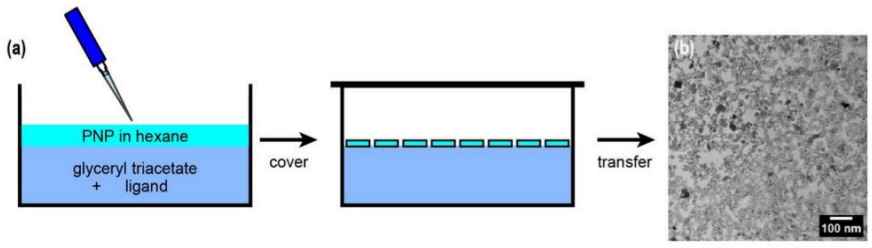

Figure 3.3. (b) Schematic of the liquid-air interfacial assembly process for anisotropic particles. For isotropic particles, additional ligand in the GTA sublayer is not necessary. (b) Film TEM.

Using this liquid-air interfacial assembly technique, we were able to achieve the same or higher surface coverage of isotropic $CsPbBr_3$ nanocrystal films on glass as compared to spin coating, and we additionally controlled long-range $CsPbBr_3$ nanoplatelet orientation into edge-up or face-down configurations. We optimized the assembly of isotropic DDAB-capped 10 nm $CsPbBr_3$ nanocubes and found that the most uniform monolayer packing was achieved by using 20 ml of GTA placed in a petri dish with 1 mL of a solution of 2.5 OD at 335 nm cast on top. This was allowed to assemble for an hour with a porous cover and then stamped on an MPTMS treated coverslip. As shown in figure 3.4, we achieved 92% monolayer surface coverage over at least a 30x30 μm area with regularly spaced patches of two monolayer stacks and sparse aggregates.

Noting the importance of a long assembly time to allow for entropy-driven nanocrystal assembly to take place, we developed a modified spin coating strategy where a larger MW solvent such as heptane or octane was used to disperse nanoparticles, and 150 μl of an OD 1.5 at 350 nm solution was used to cover the entire slip surface and allowed to sit for three minutes prior to starting spin up at 1000 rpm. We observed that this provides more time for the nanocrystals to adhere to the treated coverslip surface, and improved our surface coverage from 15% on untreated glass with no assembly time[45] to 93% over a 10x10 μm area on MPTMS treated glass with assembly time before spinning. Liquid-air interfacial assembly produces films that are more closely packed, but with some regions of multilayer stacks, whereas spin coating with assembly time yields thin films with less multilayer regions but larger voids in the film. Figure 3.5 summarizes our results of spin coating with additional assembly time and liquid-air interfacial assembly of isotropic DDAB-capped 10 nm $CsPbBr_3$ nanocrystals. Standardizing assembly to achieve uniform, monolayer films removes confounding variables of film density and aggregation

and allows for direct comparison of emission properties of nanocrystals with varying degrees of quantum confinement.

We also investigated this combined assembly time and spin coating technique for OA/OAm capped particles. Figure 3.5 shows AFM of deposited films of OA/OAm-capped $CsPbBr_3$ nanocrystals with 3.5, 5, and 10 nm edge length, as well as a film of 1:1 volume mixed 3.5 and 10 nm edge length particles. The deposition steps closely followed that of the DDAB-capped study: the solutions were diluted to ~1.6 OD at 350 nm, filtered with a 0.2 μm syringe filter, and 150 μl was cast on the surface of an MPTMS-treated coverslip. The particles were allowed to assemble for 5 minutes before spinning at 1000 rpm for 30 seconds. The OA/OAm-capped particles aggregate severely in comparison to DDAB-capped particles. All films were characterized by a sparse monolayer in the background with large, several μm wide aggregates approximately 3-5 monolayers tall. The film of combined 3.5 and 10 nm particles also demonstrated formation of nanowire-like aggregates 2-5 μm wide and nearly 100 μm tall. The surface coverage was characterized around 70-75% from AFM. Future work will focus on optimizing uniform deposition of these films, focusing on developing a DDAB exchange protocol for small particles.

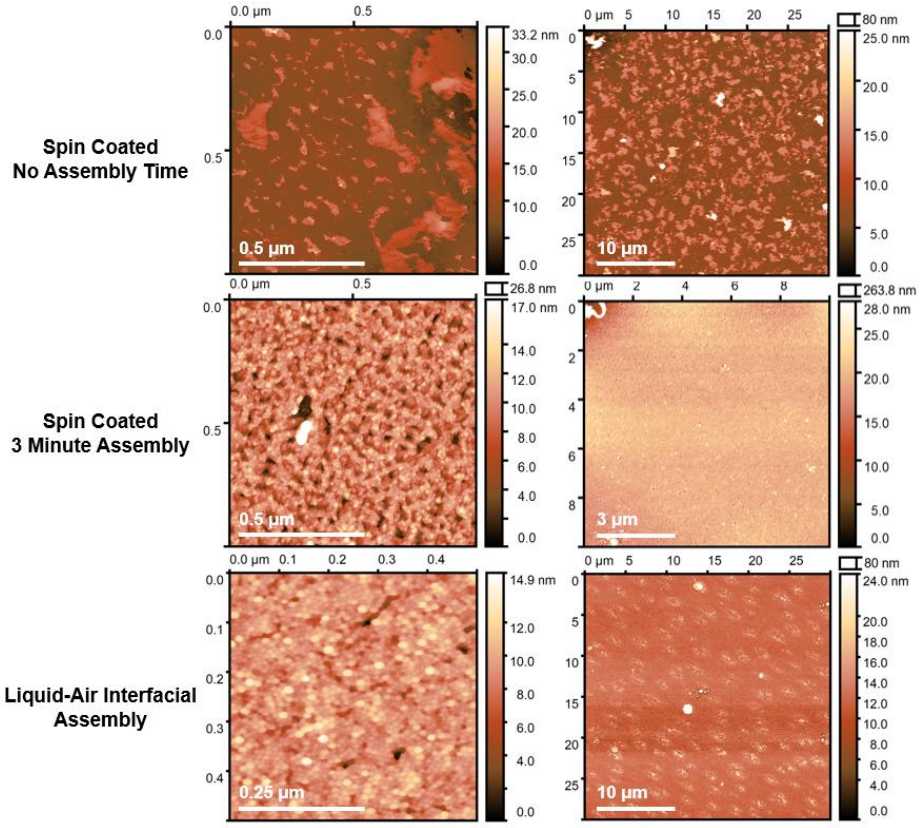

Figure 3.4. AFM images of 10 nm DDAB-capped $CsPbBr_3$ nanocrystal thin films on MPTMS treated coverslips spin coated with no assembly time, 3 minutes of assembly time, and deposited by liquid-air interfacial assembly.

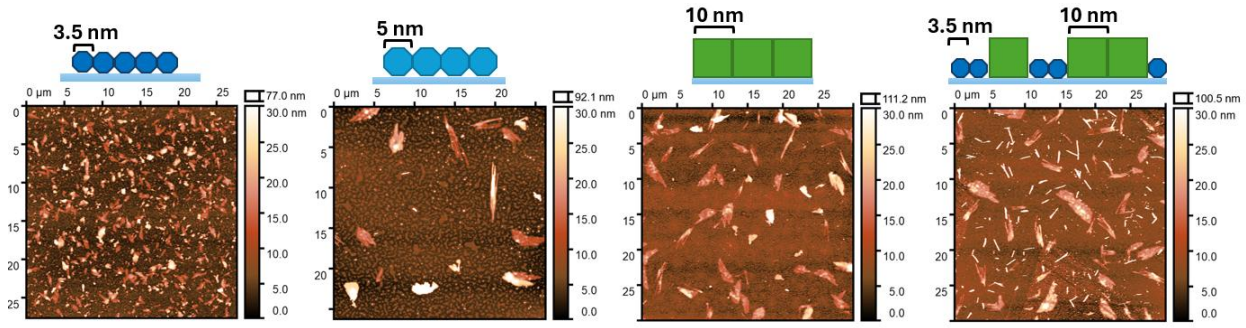

Figure 3.5. AFM of 3.5, 5, 10, and 1:1 volume mixed 3.5 and 10 nm OA/OAm-capped $CsPbBr_3$ nanocrystal thin films on MPTMS treated coverslips. These films are characterized by a sparse monolayer background overlaid with large aggregates of 3-5 monolayers.

3.2 Deposition of monolayer packed films of oriented anisotropic $CsPbBr_3$ nanocrystals

We also successfully used liquid-air interfacial assembly to control the orientation of anisotropic $CsPbBr_3$ nanoplates into face-down and edge-up regimes by controlling nanoplate volume fraction in the assembly and ligand concentration in the immiscible sublayer.[67] Face-down nanoplates occupy more surface area than edge-up ones, so we predicted that a higher volume of solution with more total particles would produce more edge-up assembly. We also hypothesized that adding oleic acid ligand into the GTA sublayer would increase the repulsive van der Waals forces between the sublayer and OA/OAm functionalized nanoplate layer, forcing more nanoplates into an edge-up regime. As shown in figure 3.6, we identified that 100 µl of a solution of nanoplates with an OD of 1.75 at 335 nm would assemble face-down, and 200 µl of the same solution with 0.68 mM OA in the sublayer would assemble edge-up. Intermediate dilutions and concentrations could produce mixed films, but volume fractions and OA concentrations that were much higher produced aggregated films.

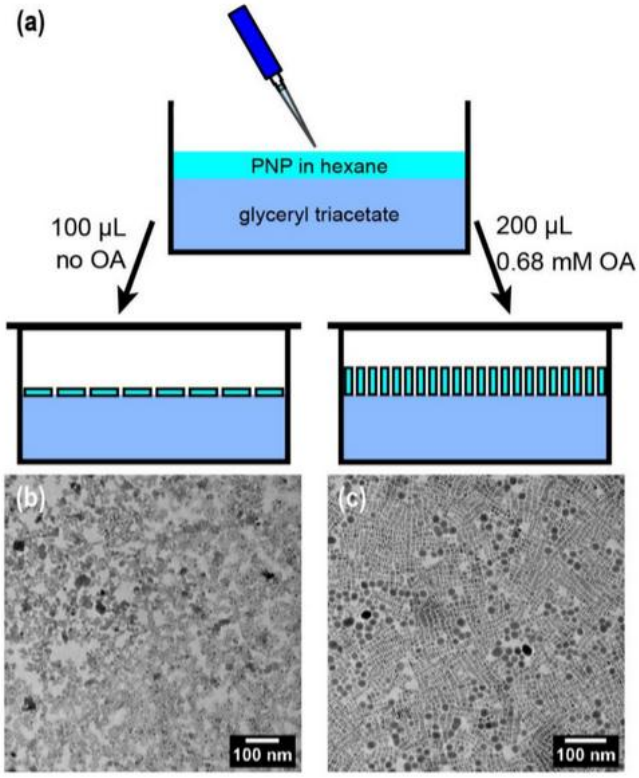

Figure 3.6. (a) Schematic of assembly at the liquid-air interface. The addition of oleic acid in the sublayer and increase in NPL volume fraction causes NPLs to assume an edge up configuration. TEM images showing $CsPbBr_3$ nanoplates assembled in a (b) face down and (c) edge up configuration.

3.3 Summary

Lead halide perovskite nanocrystal optical properties have demonstrated a wide range of tunability, allowing researchers to exploit both substrate and nanocrystal-nanocrystal interactions to tailor light emission and exciton transfer properties for optoelectronic applications. To investigate the fundamental electronic transitions leading to these properties, we deposited $CsPbBr_3$ thin films that were either single- or multi-component; ordered or disordered; and with

nanocrystal sizes in strongly and weakly quantumly confined regimes. We designed optimized deposition protocols to generate uniform monolayer thin films (>90% surface coverage) of isotropic DDAB-capped $CsPbBr_3$ nanocrystals on MPTMS treated SiO_2 free of large aggregates by spin coating or liquid-air interfacial assembly. For isotropic OA/OAm-capped $CsPbBr_3$ particles, avoiding aggregation is more challenging due to their dynamic bonding, and some aggregation was seen on the surface with the same techniques (70% surface coverage). The orientation of $CsPbBr_3$ nanoplates was controlled by using liquid-air interfacial assembly on an immiscible sublayer and by tuning both the number density of the nanoplates and ligand concentration in the sublayer. This work lays the foundation for our characterization of the film angular light emission and extraction of the dipole alignment by Fourier microscopy in the next chapter.

4. EXTRACTION OF DIPOLE ORIENTATION FROM LEAD HALIDE PEROVSKITE FILMS

To evaluate the impact of local substrate interactions and packing motif on the electronic transitions of $CsPbBr_3$ nanocrystal films, we determined the emission dipole orientation of samples with a range of nanocrystal sizes, packing densities, and assembly types. The transition dipole moment (TDM) angle describes the angle formed between the substrate plane and the vector of an electronic transition; for a film, the effective TDM angle or orientation factor dictates the angular emission by defining the electric field generated normal to the transition vector. We can create more efficient optoelectronic devices that emit primarily in desired modes by modulating effective TDM angle to achieve tuned anisotropic light emission. In contrast to traditional covalent isotropic shaped emitters, such as CdSe nanocrystals, which emit equally along two in-plane and one out-of-plane axes independent of their environment, perovskite nanocrystals show an exaggerated vertical (out-of-plane) dipole contribution on most substrates.[68] Thus, a wider range of angular emission tunability is theoretically achievable for perovskite nanocrystals. Understanding the photophysics of dipole alignment is also crucial to uncovering mechanisms behind unique properties like superfluorescence in ordered $CsPbBr_3$ nanocrystal assemblies.

Jurow et al. demonstrated an increase in effective TDM angle with decreasing $CsPbBr_3$ nanocrystal density on a polymerized hydrocarbon coated glass substrate, indicating that packing motif affects the angular emission of a perovskite film (Figure 4.1 (a)).[43] Density functional theory calculations indicated that larger particle spacing results in stronger substrate-nanocrystal interactions, increasing the impact of the charge redistribution caused by bringing two dissimilar materials in contact. The SiO_2 and perovskite have a work function mismatch (5.0 eV and 4.0 eV, respectively)[44,69] that generates charge at the interface, redistributes electrons, and exaggerates the

vertical dipole due to the ionic nature of the perovskite lattice (Figure 4.1 (b)). By analyzing the effective TDM angle of a variety of $CsPbBr_3$ films, we can develop a library of tunable parameters to both control angular emission and better understand the fundamental properties of electronic transitions in these unique materials.

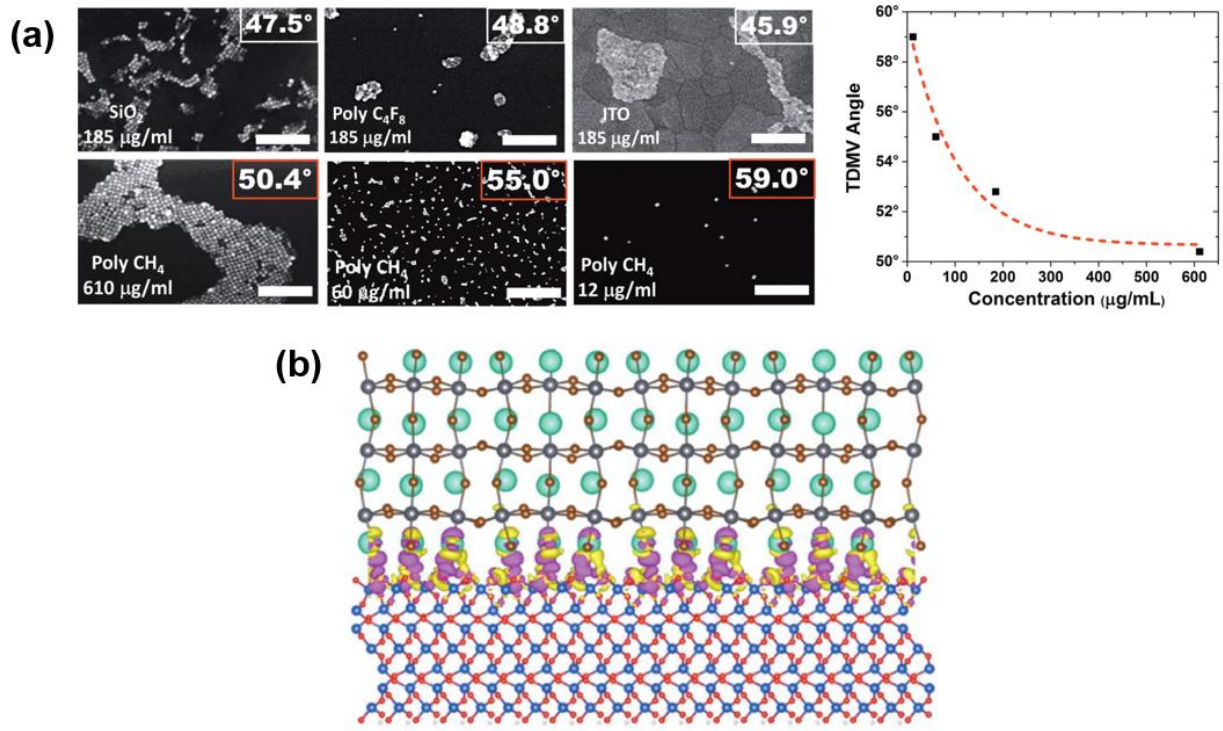

Figure 4.1. (a) SEM images of films of $CsPbBr_3$ nanocubes self-assembled on coated surfaces. The angle between the substrate and the TDM are inset, and an exponential fit is shown with the dashed red line (scale bars: 200 nm). (b) Density functional theory modeling the effect of bringing the cubic perovskite lattice into approximate contact with an SiO_2 substrate shows a redistribution of the electron densities near the interface, introducing a small electrical field. From Jurow et al.[43]

4.1 Back Focal Plane Fluorescence Microscopy (BFPFM) experiment and theory

We utilized back focal plane fluorescence microscopy (BFPFM), also known as Fourier microscopy,[70] to resolve angular emission patterns and determine effective TDM angle for densely packed films (>50% surface nanocrystal coverage). BFPFM was performed using a home-built inverted microscope with excitation by a 405 nm continuous wave laser and a 100x oil immersion objective, depicted in figure 4.2. The focal plane in a wide-field imaging fluorescence microscope was transformed from the sample plane to the Back Focal Plane by inserting a Bertrand Lens between the objective and the tube lens.[70] We used a linear polarizer to decouple the k_x and k_y signal and longpass filters to isolate photoluminescence from the films and remove laser signal.

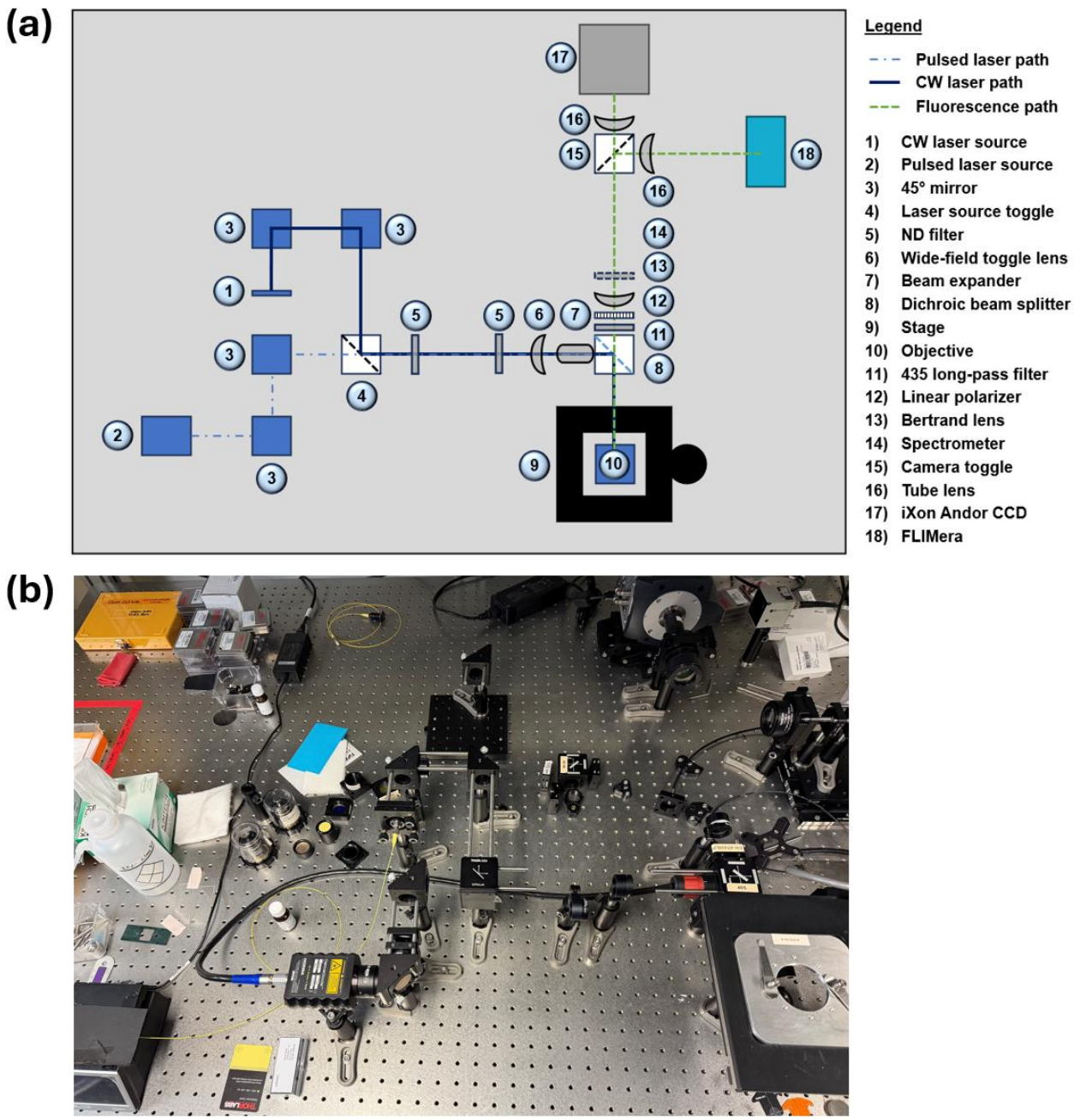

Figure 4.2. Schematic (a) and photo (b) of BFPFM imaging setup where the sample is excited by a 405 nm laser source, emission is magnified 100x by the objective, then polarized, transformed to momentum space, and captured on a CCD.

Back focal plane (BFP) images depict a 2D projection of the 3D angular emission pattern of the nanocrystal film. Figure 4.3 (a) demonstrates how an increasing TDM angle manifests in polarized BFP images, with a 0° TDM angle representing a fully forward-propagating emission mode perpendicular to the substrate and a 90° TDM angle representing a fully parallel-propagating emission mode parallel to the substrate. We were able to determine vertical and horizontal dipole contributions from a sample by fitting the collected patterns to a three-layer model which determines the angular emission pattern resulting from a film on a substrate surrounded by air. The three layers are the substrate (glass), the emissive layer ($CsPbBr_3$ film), and the surrounding air. The intensity of emitted light projected onto a 2D collection plane (N_{pol}) as a function of photon momentum vectors along the x- and y- directions (k_x, k_y) is described by the following equation[44,71]

$$N^{pol}(k_x, k_y) = C\left[\left(\rho_{IP}^{p} + \rho_{IP}^{s}\right)\frac{1-\sin^2(\phi)}{2} + \rho_{OP}^{p}\sin^2(\phi)\right]$$

Where C is a normalization constant arising from the integration time of the collection media and excitation intensity, ρ_{ip}^{s} and ρ_{ip}^{p} are the density of states s- and p-polarized in-plane dipole contributions, ρ_{op}^{p} is the out-of-plane dipole contribution. Density of states is a function of the photoluminescence wavelength, refractive indices of the layers, and the thickness of the emissive layer. The density of states in each direction is given by:

$$\rho_{IP}^{s} = \rho_{y}^{s}(k_x, k_y) = \left(\frac{1}{8\pi k_0^2}\right)\left(\frac{k_0}{k_{z,3}}\right)\left|\frac{t_{32}^{s} e^{\frac{ik_{z,2}D}{2}}\left(1 + r_{21}^{s} e^{ik_{z,2}D}\right)}{1 - r_{21}^{s} r_{23}^{s} e^{2ik_{z,2}D}}\frac{k_y}{\sqrt{k_x^2 + k_y^2}}\right|^2$$

$$\rho_{IP}^{p} = \rho_{x}^{p}(k_x, k_y) = \left(\frac{1}{8\pi k_0^2}\right)\left(\frac{k_0}{k_{z,3}}\right)\left|\frac{t_{32}^{p} e^{\frac{ik_{z,2}D}{2}}\left(1 - r_{21}^{p} e^{ik_{z,2}D}\right)\frac{k_{z,2}}{n_2 k_0}}{1 - r_{21}^{p} r_{23}^{p} e^{2ik_{z,2}D}}\frac{k_x}{\sqrt{k_x^2 + k_y^2}}\right|^2$$

$$\rho_{OP}^{p} = \rho_{z}^{s}(k_x, k_y) = \left(\frac{1}{8\pi k_0^2}\right)\left(\frac{k_0}{k_{z,3}}\right)\left|\frac{t_{32}^{p} e^{\frac{ik_{z,2}D}{2}}\left(1 + r_{21}^{p} e^{ik_{z,2}D}\right)\frac{k_x}{n_2 k_0}}{1 - r_{21}^{p} r_{23}^{p} e^{2ik_{z,2}D}}\right|^2$$

where

$$k_0 = \frac{2\pi}{\lambda}$$

$$k_{z,i} = \sqrt{n_i^2 k_0^2 - \left(k_x^2 + k_y^2\right)}$$

Here, λ is the emitted light wavelength, n_i is the refractive index of layer i, t_{ij}^{l} is the Fresnel transmission coefficient between regions i and j for l-polarized light, r_{ij}^{l} is the Fresnel reflection coefficient between regions i and j for l-polarized light, and D is the thickness of the emitter layer. The Fresnel coefficients account for light that is reflected at each boundary between regions. This model allows us to calculate the theoretical emission signal and compare it to our collected BFP images. The images are fit to theoretical parameters by a chi^2 minimization according to Russ et al.[35] to determine an effective TDM angle of best fit by adjusting input refractive index, emission wavelength, and film thickness parameters.

Figure 4.3 (a) depicts a schematic of the three-layer model used for BFPFM image modeling. Figure 4.3 (c) shows how a BFP image transforms as effective TDM angle changes; this evolution is most evident in the horizontal p-polarized cross section at k_y=0. As effective TDM angle increases from 0° to 90°, the signal at $|k_x|$=1 changes from a sharp decrease to 0 to a smoother curve and the signal at $|k_x|$>1 increases. Whereas the horizontal cross-section intensity depends on effective TDM angle alignment, it is important to note that the vertical s-polarized cross section at k_x = 0 is only a weak function of dipole alignment angle and depends mostly on the emissive layer

thickness, refractive index, and wavelength (Figure 4.3 (d-e)). These model images represent a range of dipole contributions; equal contributions from two horizontal and one vertical dipole would lead to an effective TDM angle of 35°. Such isotropic emission can be seen naturally in randomly ordered assemblies of isotropically shaped emitters such as CdSe quantum dots.

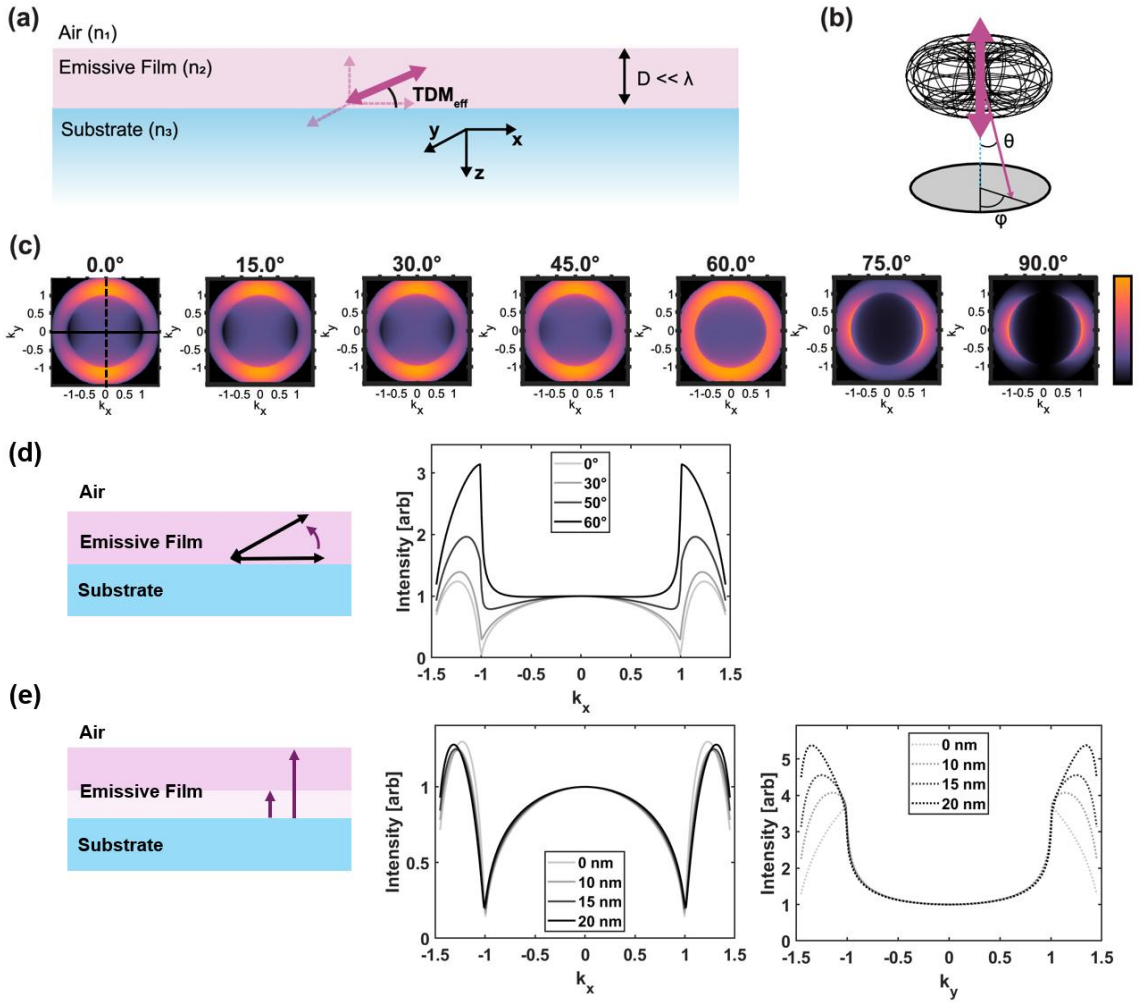

Figure 4.3. (a) Three-layer schematic used for modeling BFPFM showing air, emissive film, and the substrate. The thickness of the film is generally assumed to be smaller than the emission wavelength of light. The effective TDM angle is between the substrate and in-plane and out-of-plane dipole contributions, which are shown in pink. (b) Wireframe angular emission pattern (black) from a dipole (purple), with emission defined in spherical coordinates (θ, ϕ). (c) Polarized

BFPFM signal modeled for a thin film with a given effective transition dipole moment from 0° to 90°. Changes in the image are slight for effective TDM angle ≤ 30°. (a)-(c) Used with permission from Russ et al.[35] (d) Cross-sections showing how changing TDM angle reflects in the k_x signal for a 0 nm thick film. (e) Cross-sections showing how increasing thickness changes the k_x and k_y signal for a TDM angle of 20°.

When fitting collected BFP images to theoretical model simulations, it is important to provide an appropriate estimated range for the film thickness, refractive index, and emission wavelength. For our model, we used the appropriate center wavelength for the emitting $CsPbBr_3$ nanocrystal sample, a refractive index estimated using the effective medium approximation from both TEM and AFM, and a film thickness of 0 nm which is appropriate for sparse films much thinner than the wavelength of light. Film uniformity is also crucial as calculations are based on a homogeneous emissive layer. In fitting BFP images from oriented CdSe nanoplates, Gao et al. observed that good agreement between simulated and experimental BFP images was only obtained if data was collected from thin film sample regions with homogeneous emission intensity (Figure 4.4).[42]

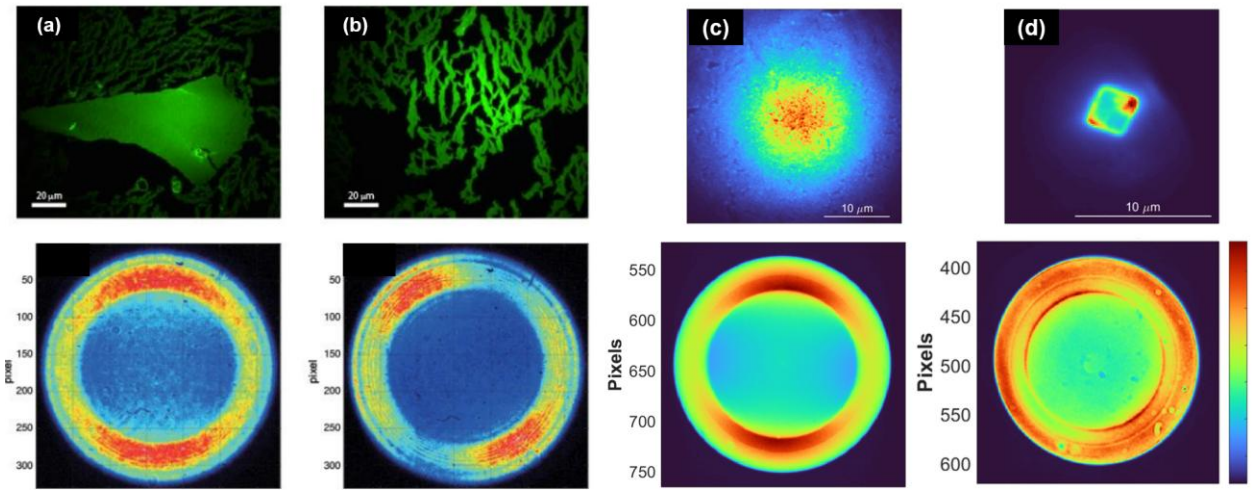

Figure 4.4. Wide-field fluorescence image (top) and associated back focal plane image (bottom) from homogenous monolayer region of CdSe (a) and $CsPbBr_3$ (c) nanocrystals, CdSe sparse region (b), (adapted from Gao et al.[72]) and $CsPbBr_3$ superlattice assembly (d) (used with permission from Brendan Russ). Good agreement with simulated images is only achieved from homogenous thin film regions (a,c).

4.2 TDM angle extraction from assembled $CsPbBr_3$ thin films

To tune angular emission using anisotropic particles, we controlled the orientation of $CsPbBr_3$ nanoplates by changing both nanocrystal volume fraction and ligand concentration in the GTA sublayer as we reported in Parsons et al.[67] For ideal, completely confined 2D plates a face-down assembly would be expected to have a TDM angle of 0° with dipoles oriented in-plane; 2D plates oriented edge up would have an expected TDM angle of 45°. Here, 4 ± 1 nm thick plates synthesized by a hot injection synthesis adapted from Bertolotti et al.[54] and Bekenstein et al.[73] were assembled either face-down or edge-up using liquid-air interfacial assembly on a glyceryl triacetate sublayer. By adding additional oleic acid into the sublayer and increasing the

concentration of nanoplates in solution, a larger fraction of edge up assembly was achieved. The face-down plates were found to have an effective TDM angle of 28 ± 2°, higher than the ideal 0° due to the plates being only lightly confined, which meant that transitions along the out-of-plane dimension were not completely eliminated. Edge up plates demonstrated a fit effective TDM angle of 46 ± 2°, higher than the ideal value due to interfacial charging at the SiO_2 surface. (Figure 4.5 (a-b)) We demonstrated that thermodynamically controlled nanocrystal assembly is possible for perovskite nanocrystals, permitting further tunability of angular emission from semiconductor nanocrystals for use in devices that require specific emission modes such as solar concentrating technologies or LEDs. In the future, this technique could be applied to more confined nanoplates or to different substrates to further push the limits of achievable effective TDM angles.

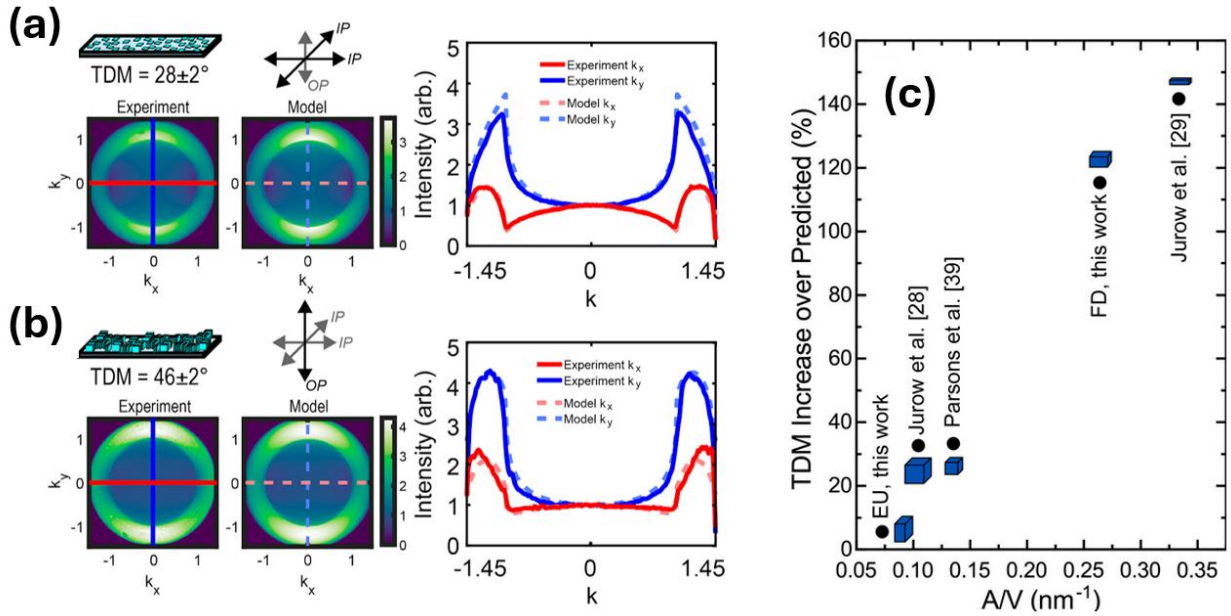

Figure 4.5. (a) Collected BFPFM signal, modeled signal of best fit, and extracted k_x (red) and k_y (blue) cross sections for face-down assemblies with an effective TDM angle of the ensemble at 28 ± 2° or Θ = 0.78, corresponding to stronger in-plane dipole contributions. (b) Collected BFPFM

signal, modeled signal of best fit, and extracted k_x (red) and k_y (blue) cross sections for edge-up assemblies with an effective TDM angle of the ensemble at 46 ± 2° or Θ = 0.48, corresponding to stronger out-of-plane dipole contributions. (c) Increase in TDM angle of a monolayer of $CsPbBr_3$ nanocubes and nanoplates on glass compared to theoretical predictions for this work and prior work, plotted against particle contact area with the substrate scaled by particle volume (nm^{-1}).

It was evident from the results of this study that the contact area of $CsPbBr_3$ nanocrystals with the substrate impacts the effective TDM angle of the film (Figure 4.5 (c)), leading us to investigate dipole alignment in isotropic quantumly confined nanocrystal films that have a large portion of their total volume in contact with the substrate. We collected experimental BFP images for $CsPbBr_3$ nanocrystal films in both strongly confined and unconfined regimes. Nanocrystals with an edge length of 3.5 nm and colloidal CWL 467 nm (strongly quantumly confined), edge length of 5 nm and colloidal CWL 490 (intermediately confined), and 10 nm with CWL 515 (unconfined) were synthesized using the method from Akkerman et al. and deposited in the manner described in chapter 3. BFPFM images were collected from each sample and fit to theoretical data. For fitting, a thickness range from 0-20 nm was allowed, along with the emission wavelength specific to each nanocrystal size, and a refractive index allowed to vary from 1.8 to 2.0, representing a surface coverage of approximately 70% found from AFM. The 3.5 nm edge length film was fit to near identical effective TDM angles of 40±5°, 5 nm to 40±5°, and the 10 nm 41±5°, with a film thickness of 0 nm for all (Figure 4.6). A film of equal volume of 3.5 and 10 nm particles mixed was also deposited and imaged using a 500 short and long pass filter to isolate emission from each particle size; both BFP datasets fit to the same angle of 41±5° and a film thickness of 6-10 nm (Figure 4.7). The error of 5° is derived from confidence intervals established by Monte

Carlo simulations performed by Russ et al. for fitting of all three parameters (RI, thickness, TDM angle) for a 10 nm film and a refractive index of 1.5-2.0.[35]

Although we hypothesized that small nanocrystals would exhibit an enhanced vertical dipole contribution due to their large surface area to volume ratio and resulting increased sensitivity to substrate work function mismatch, interparticle interactions likely dominate for packed films regardless of quantum confinement. The vertical dipole contribution of these films was also less than anticipated, with an angle of 47° reported previously for sparse isotropic $CsPbBr_3$ nanocube monolayers with 15% surface coverage.[35] The same work also saw a reduction in effective TDM angle from 47° for sparse nanocubes (15% coverage) to 44° for higher coverage mixed nanocube and nanoplate films (34% coverage). This supports that the results below are likely due to higher surface coverage and film aggregation visible in figure 3.6, where thicker, aggregated parts of the film are less affected by substrate surface charge redistribution and the TDM angle is thus pushed down towards an isotropic emission angle of 35.3°. Future work will emphasize creating uniform thin films of different sized particles and take advantage of dilution or polymer substrates to exaggerate the effects of increased substrate contact.

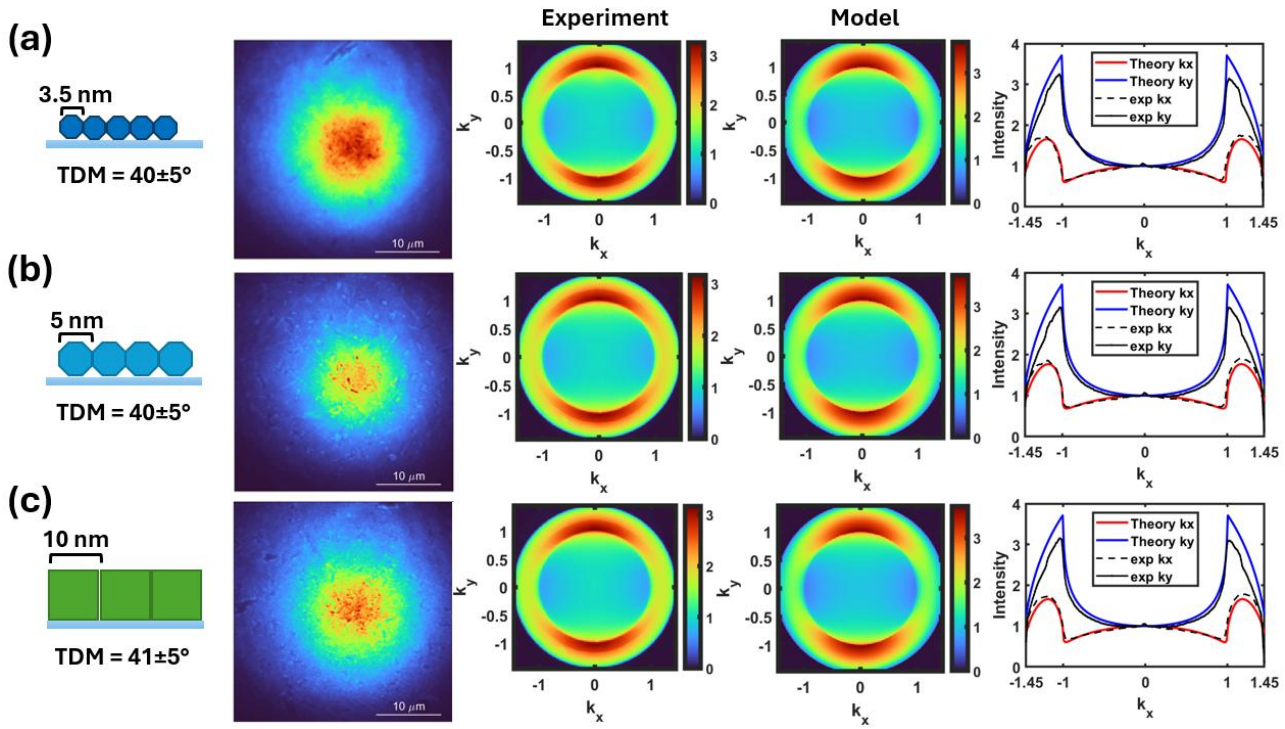

Figure 4.6. Wide-field, model fit and experimental BFP images along with TDM angle of films of 3.5 (a), 5 (b), and 10 (c) nm $CsPbBr_3$ nanocrystals.

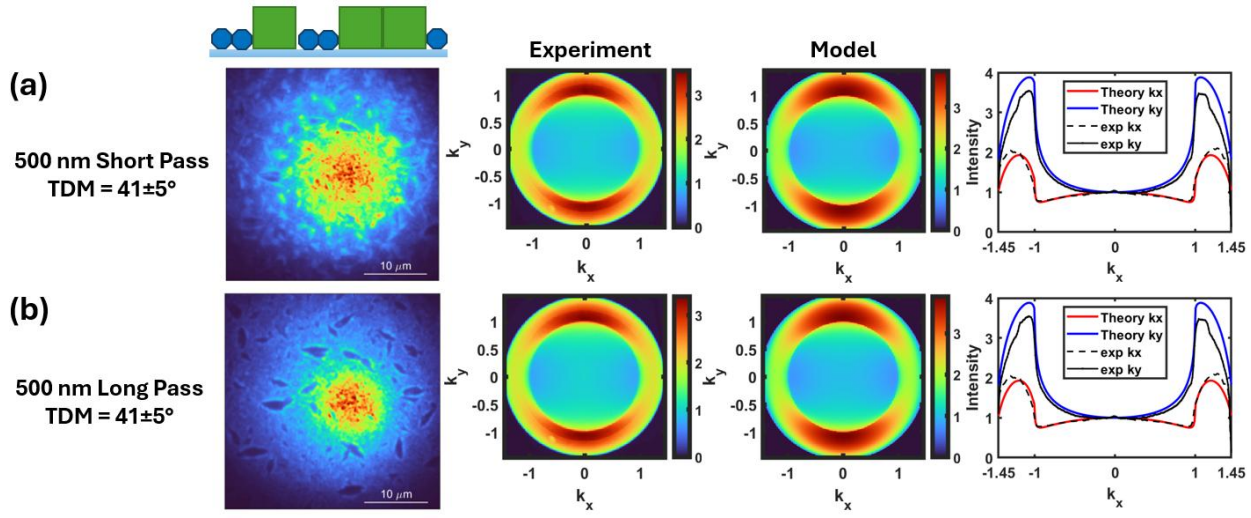

Figure 4.7. Wide-field, model fit and experimental BFP images along with TDM angle of films of mixed 3.5 and 10 nm $CsPbBr_3$ nanocrystals imaged with a 500 nm short (a) and long (b) pass lens to isolate emission from each nanocrystal size.

4.3 Summary

We captured the angular emission patterns of thin films assembled from a variety of nanocrystal sizes, ordered or disordered motifs, and anisotropic particle orientations. These patterns, obtained by either Back Focal Plane Fluorescence Microscopy (BFPFM), were created by introducing aberration into the light path either by a Bertrand Lens. Using BFPFM we can extract information about film or nanocrystal dipole alignment, which dictates angular emission, by fitting experimental images to model generated images using a chi^2 minimization and extracting an effective TDM angle value for dense films. Isotropic nanocrystal thin films exhibited nearly identical effective TDM angles (~40–41°) across strongly quantumly confined and unconfined size regimes, indicating that interparticle interactions in dense films dominate over size-mediated substrate effects. Anisotropic nanoplates demonstrated substantial tunability, with effective TDM angles varying from ~28° in face-down assemblies to ~46° in edge-up configurations. Information about the dipole alignment in a sample informs us about the fundamental electronic transitions happening within the assembly and permits us to push the limits of achievable TDM angles for next generation optoelectronic devices.

5. CONCLUSION

In this work, we investigated how the light emission of colloidal lead halide perovskite nanocrystals can be controlled through manipulation of their morphology and structural environment. As semiconductor nanocrystals reach near-unity photoluminescence quantum yields, further improvements in optoelectronic performance depend increasingly on directing emitted photons rather than enhancing intrinsic radiative efficiency. We characterized the extent of dipole alignment tunability by extracting the effective transition dipole moment (TDM) angle, which governs angular emission. By integrating synthetic optimization, ligand engineering, controlled film assembly, and optical microscopy, we developed methods to engineer dipole orientation in $CsPbBr_3$ nanocrystal films.

We investigated several synthetic protocols to create $CsPbBr_3$ nanocrystals spanning strongly quantum confined to unconfined regimes (3.5–13 nm) and were able to achieve size- and shape-uniform samples in ambient conditions. We optimized purification protocols to permit extraction of synthesized nanocrystals while maintaining colloidal stability and preventing aggregation. In parallel, we also evaluated multiple ligand chemistries, including OA/OAm, DDAB, and lecithin, to analyze the balance between surface passivation strength, colloidal stability, and compatibility with ordered self-assembly. These optimizations provided a set of reproducible materials techniques for controlled nanocrystal thin film deposition.

We fabricated of close-packed monolayers and oriented nanoplate assemblies using spin coating and liquid-air interfacial assembly. Substrate functionalization improved film uniformity, while liquid–air interfacial assembly enabled long-range ordering and controlled nanoplate orientation. Angular emission of the films was quantified using Back Focal Plane Fluorescence Microscopy (BFPFM) and fit to a three-layer model to extract effective film TDM. Isotropic

nanocube monolayers exhibited nearly identical effective TDM angles (~40–41±5°) across different nanocrystal sizes from 3.5-10 nm, as well as binary films of 3.5 and 10 nm nanocrystals, indicating that collective interparticle interactions dominate over quantum confinement effects in dense films. We demonstrated effective tunability of nanoplate angular emission by controlling the orientation of the nanoplates withing the film, with effective TDM angles of 28 ± 2° (face-down) and 46 ± 2° (edge-up).

Looking forward, several directions for future work have been established. Creating uniform films of mixed particle sizes by minimizing aggregation will allow us to more fully analyze the effects of increased substrate contact in quantumly confined films. Extending controlled assembly strategies to more strongly confined two-dimensional platelets and alternative substrates will provide opportunities to achieve even greater tunability of dipole alignment. Improving our microscope instrument capabilities for single-nanocrystal imaging will enable direct observation of dipole alignment of isolated particles. These efforts will collectively expand our ability to design light-emitting films with precise angular emission control, informing the development of high-efficiency LEDs, luminescent solar concentrators, and quantum photonic devices where photon directionality and coherence are critical.

Appendices

Appendix A: Lecithin NMR Spectra

Reference Spectra

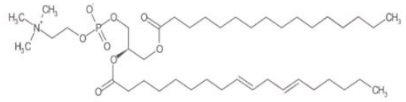

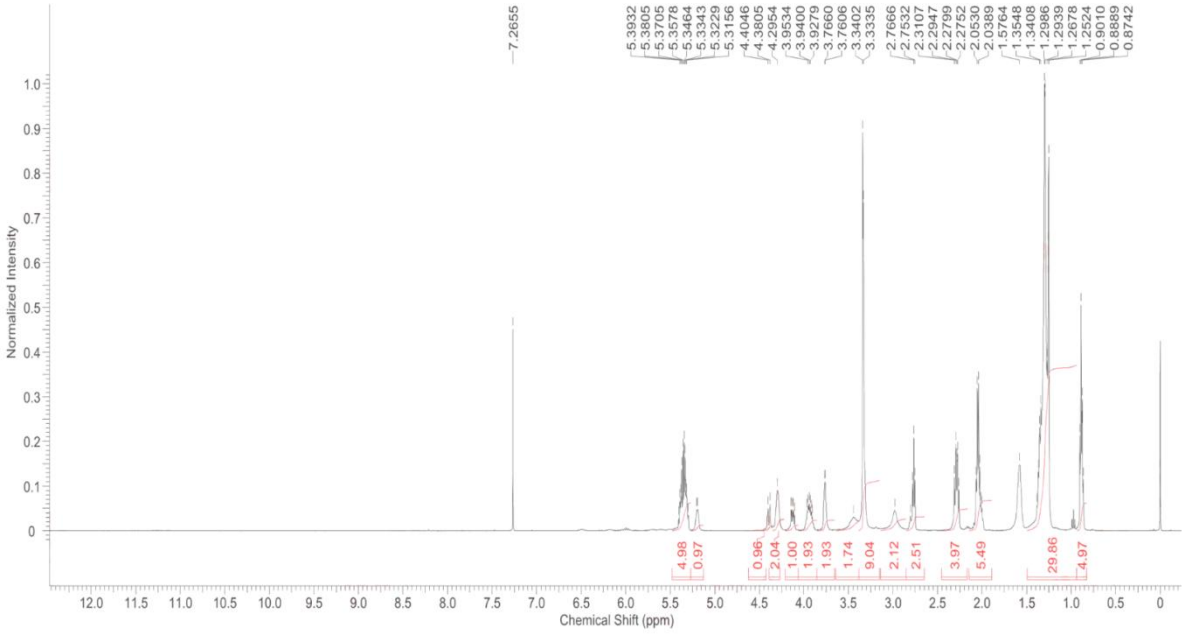

Refined Lecithin - Fisher

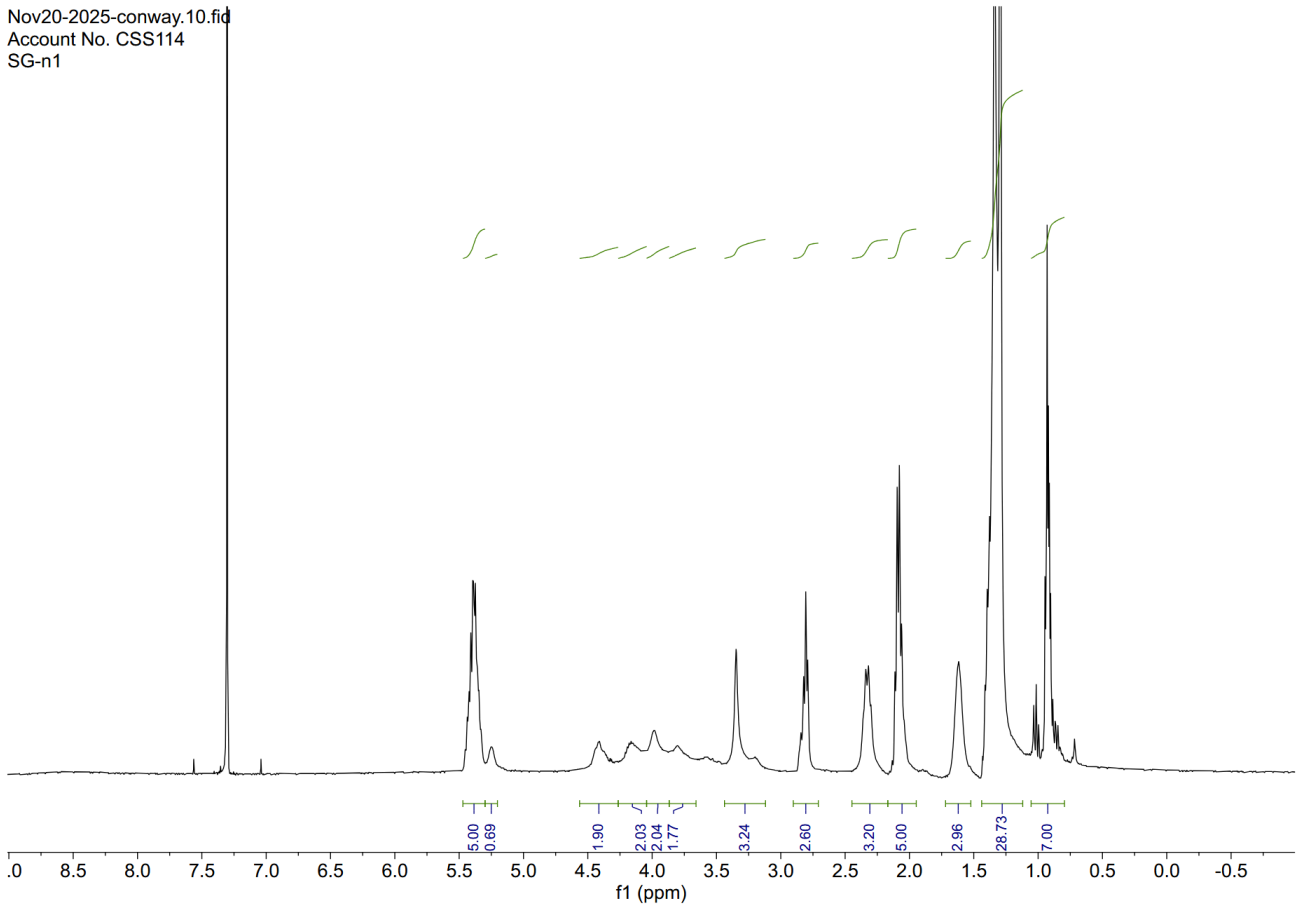

Granular Lecithin 97% - Fisher

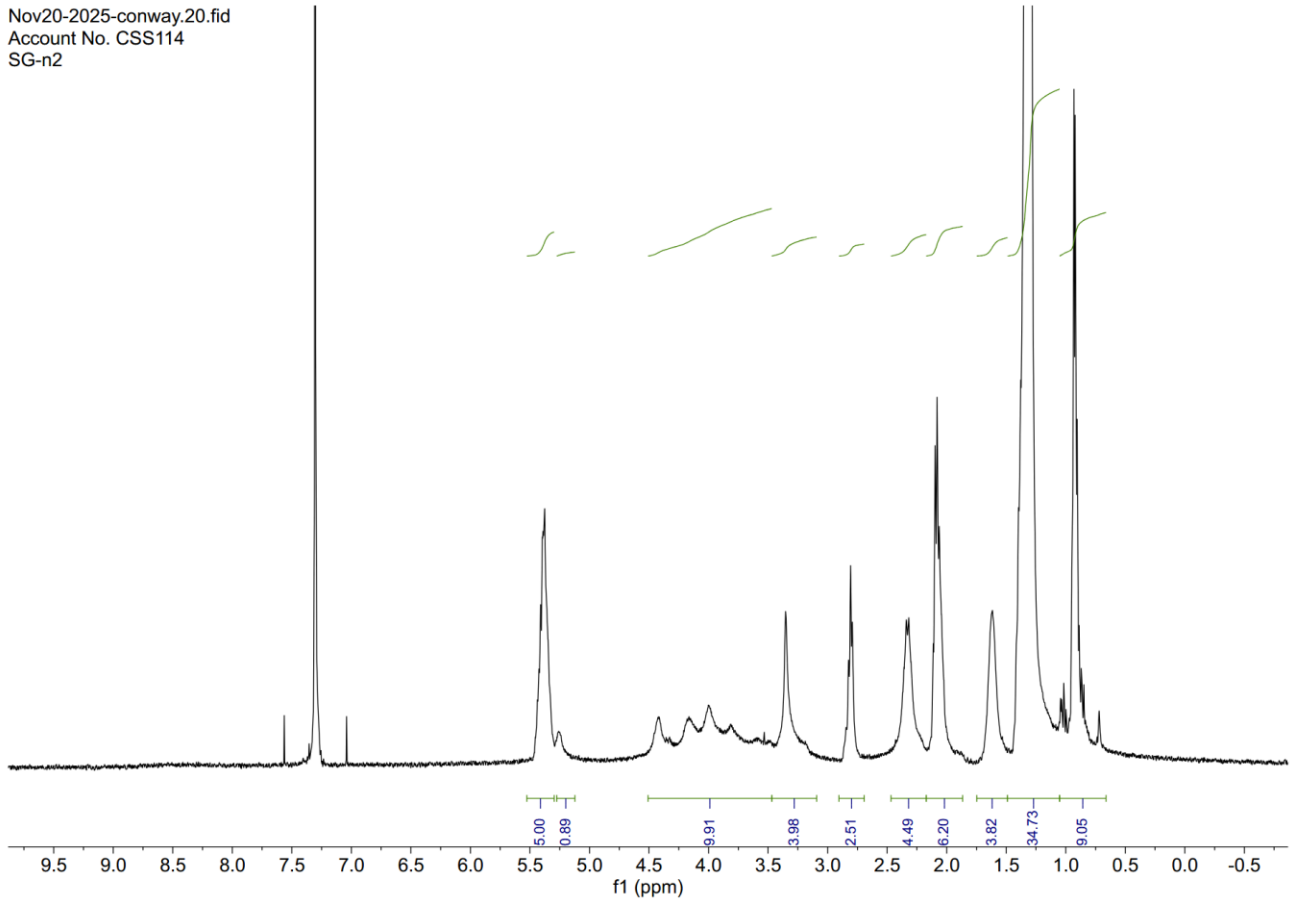

References

(1) Zhu, J.; Li, Y.; Lin, X.; Han, Y.; Wu, K. Coherent Phenomena and Dynamics of Lead Halide Perovskite Nanocrystals for Quantum Information Technologies. *Nat. Mater.* **2024**, *23* (8), 1027–1040. https://doi.org/10.1038/s41563-024-01922-z.

(2) Ibáñez, M.; Boehme, S. C.; Buonsanti, R.; De Roo, J.; Milliron, D. J.; Ithurria, S.; Rogach, A. L.; Cabot, A.; Yarema, M.; Cossairt, B. M.; Reiss, P.; Talapin, D. V.; Protesescu, L.; Hens, Z.; Infante, I.; Bodnarchuk, M. I.; Ye, X.; Wang, Y.; Zhang, H.; Lhuillier, E.; Klimov, V. I.; Utzat, H.; Rainò, G.; Kagan, C. R.; Cargnello, M.; Son, J. S.; Kovalenko, M. V. Prospects of Nanoscience with Nanocrystals: 2025 Edition. *ACS Nano* **2025**, *19* (36), 31969–32051. https://doi.org/10.1021/acsnano.5c07838.

(3) Yakunin, S.; Protesescu, L.; Krieg, F.; Bodnarchuk, M. I.; Nedelcu, G.; Humer, M.; De Luca, G.; Fiebig, M.; Heiss, W.; Kovalenko, M. V. Low-Threshold Amplified Spontaneous Emission and Lasing from Colloidal Nanocrystals of Caesium Lead Halide Perovskites. *Nat. Commun.* **2015**, *6* (1), 8056. https://doi.org/10.1038/ncomms9056.

(4) Yassitepe, E.; Yang, Z.; Voznyy, O.; Kim, Y.; Walters, G.; Castañeda, J. A.; Kanjanaboos, P.; Yuan, M.; Gong, X.; Fan, F.; Pan, J.; Hoogland, S.; Comin, R.; Bakr, O. M.; Padilha, L. A.; Nogueira, A. F.; Sargent, E. H. Amine-Free Synthesis of Cesium Lead Halide Perovskite Quantum Dots for Efficient Light-Emitting Diodes. *Adv. Funct. Mater.* **2016**, *26* (47), 8757–8763. https://doi.org/10.1002/adfm.201604580.

(5) Meinardi, F.; Akkerman, Q. A.; Bruni, F.; Park, S.; Mauri, M.; Dang, Z.; Manna, L.; Brovelli, S. Doped Halide Perovskite Nanocrystals for Reabsorption-Free Luminescent Solar Concentrators. *ACS Energy Lett.* **2017**, *2* (10), 2368–2377. https://doi.org/10.1021/acsenergylett.7b00701.

(6) Yakunin, S.; Chaaban, J.; Benin, B. M.; Cherniukh, I.; Bernasconi, C.; Landuyt, A.; Shynkarenko, Y.; Bolat, S.; Hofer, C.; Romanyuk, Y. E.; Cattaneo, S.; Pokutnyi, S. I.; Schaller, R. D.; Bodnarchuk, M. I.; Poulikakos, D.; Kovalenko, M. V. Radiative Lifetime-Encoded Unicolour Security Tags Using Perovskite Nanocrystals. *Nat. Commun.* **2021**, *12* (1), 981. https://doi.org/10.1038/s41467-021-21214-3.

(7) Protesescu, L.; Yakunin, S.; Bodnarchuk, M. I.; Krieg, F.; Caputo, R.; Hendon, C. H.; Yang, R. X.; Walsh, A.; Kovalenko, M. V. Nanocrystals of Cesium Lead Halide Perovskites ($CsPbX_3$, X = Cl, Br, and I): Novel Optoelectronic Materials Showing Bright Emission with Wide Color Gamut. *Nano Lett.* **2015**, *15* (6), 3692–3696. https://doi.org/10.1021/nl5048779.

(8) Cahill, J. T.; Graeve, O. A. Hexaborides: A Review of Structure, Synthesis and Processing. *J. Mater. Res. Technol.* **2019**, *8* (6), 6321–6335. https://doi.org/10.1016/j.jmrt.2019.09.041.

(9) Mackinnon, I. D. R.; Alarco, J. A.; Talbot, P. C. Metal Hexaborides with Sc, Ti or Mn. *Model. Numer. Simul. Mater. Sci.* **2013**, *03* (04), 158–169. https://doi.org/10.4236/mnsms.2013.34023.

(10) R. Heath, J. Covalency in Semiconductor Quantum Dots. *Chem. Soc. Rev.* **1998**, *27* (1), 65. https://doi.org/10.1039/a827065z.

(11) Li, Y.; Hou, X.; Dai, X.; Yao, Z.; Lv, L.; Jin, Y.; Peng, X. Stoichiometry-Controlled InP-Based Quantum Dots: Synthesis, Photoluminescence, and Electroluminescence. *J. Am. Chem. Soc.* **2019**, *141* (16), 6448–6452. https://doi.org/10.1021/jacs.8b12908.

(12) Russ, B.; Eisler, C. N. The Future of Quantum Technologies: Superfluorescence from Solution-Processed, Tunable Materials. *Nanophotonics* **2024**, *13* (11), 1943–1951. https://doi.org/10.1515/nanoph-2023-0919.

(13) Protesescu, L.; Yakunin, S.; Bodnarchuk, M. I.; Bertolotti, F.; Masciocchi, N.; Guagliardi, A.; Kovalenko, M. V. Monodisperse Formamidinium Lead Bromide Nanocrystals with Bright and Stable Green Photoluminescence. *J. Am. Chem. Soc.* **2016**, *138* (43), 14202–14205. https://doi.org/10.1021/jacs.6b08900.

(14) Chen, J.-K.; Zhang, B.-B.; Liu, Q.; Shirahata, N.; Mohammed, O. F.; Bakr, O. M.; Sun, H.-T. Advances and Challenges in Tin Halide Perovskite Nanocrystals. *ACS Mater. Lett.* **2021**, *3* (11), 1541–1557. https://doi.org/10.1021/acsmaterialslett.1c00444.

(15) Sharif, R.; Khalid, A.; Ahmad, S. W.; Rehman, A.; Qutab, H. G.; Akhtar, H. H.; Mahmood, K.; Afzal, S.; Saleem, F. A Comprehensive Review of the Current Progresses and Material Advances in Perovskite Solar Cells. *Nanoscale Adv.* **2023**, *5* (15), 3803–3833. https://doi.org/10.1039/D3NA00319A.

(16) Li, G.; Tan, Z.-K.; Di, D.; Lai, M. L.; Jiang, L.; Lim, J. H.-W.; Friend, R. H.; Greenham, N. C. Efficient Light-Emitting Diodes Based on Nanocrystalline Perovskite in a Dielectric Polymer Matrix. *Nano Lett.* **2015**, *15* (4), 2640–2644. https://doi.org/10.1021/acs.nanolett.5b00235.

(17) Kang, C. H.; Dursun, I.; Liu, G.; Sinatra, L.; Sun, X.; Kong, M.; Pan, J.; Maity, P.; Ooi, E.-N.; Ng, T. K.; Mohammed, O. F.; Bakr, O. M.; Ooi, B. S. High-Speed Colour-Converting Photodetector with All-Inorganic CsPbBr3 Perovskite Nanocrystals for Ultraviolet Light Communication. *Light Sci. Appl.* **2019**, *8* (1), 94. https://doi.org/10.1038/s41377-019-0204-4.

(18) Chen, Q.; Wu, J.; Ou, X.; Huang, B.; Almutlaq, J.; Zhumekenov, A. A.; Guan, X.; Han, S.; Liang, L.; Yi, Z.; Li, J.; Xie, X.; Wang, Y.; Li, Y.; Fan, D.; Teh, D. B. L.; All, A. H.; Mohammed, O. F.; Bakr, O. M.; Wu, T.; Bettinelli, M.; Yang, H.; Huang, W.; Liu, X. All-

Inorganic Perovskite Nanocrystal Scintillators. *Nature* **2018**, *561* (7721), 88–93. https://doi.org/10.1038/s41586-018-0451-1.

(19) Swarnkar, A.; Marshall, A. R.; Sanehira, E. M.; Chernomordik, B. D.; Moore, D. T.; Christians, J. A.; Chakrabarti, T.; Luther, J. M. Quantum Dot–Induced Phase Stabilization of α-$CsPbI_3$ Perovskite for High-Efficiency Photovoltaics. *Science* **2016**, *354* (6308), 92–95. https://doi.org/10.1126/science.aag2700.

(20) Akkerman, Q. A.; Nguyen, T. P. T.; Boehme, S. C.; Montanarella, F.; Dirin, D. N.; Wechsler, P.; Beiglböck, F.; Rainò, G.; Erni, R.; Katan, C.; Even, J.; Kovalenko, M. V. Controlling the Nucleation and Growth Kinetics of Lead Halide Perovskite Quantum Dots. *Science* **2022**, *377* (6613), 1406–1412. https://doi.org/10.1126/science.abq3616.

(21) Protesescu, L.; Yakunin, S.; Bodnarchuk, M. I.; Krieg, F.; Caputo, R.; Hendon, C. H.; Yang, R. X.; Walsh, A.; Kovalenko, M. V. Nanocrystals of Cesium Lead Halide Perovskites ($CsPbX_3$, X = Cl, Br, and I): Novel Optoelectronic Materials Showing Bright Emission with Wide Color Gamut. *Nano Lett.* **2015**, *15* (6), 3692–3696. https://doi.org/10.1021/nl5048779.

(22) Brown, A. A. M.; Vashishtha, P.; Hooper, T. J. N.; Ng, Y. F.; Nutan, G. V.; Fang, Y.; Giovanni, D.; Tey, J. N.; Jiang, L.; Damodaran, B.; Sum, T. C.; Pu, S. H.; Mhaisalkar, S. G.; Mathews, N. Precise Control of $CsPbBr_3$ Perovskite Nanocrystal Growth at Room Temperature: Size Tunability and Synthetic Insights. *Chem. Mater.* **2021**, *33* (7), 2387–2397. https://doi.org/10.1021/acs.chemmater.0c04569.

(23) Bodnarchuk, M. I.; Boehme, S. C.; Ten Brinck, S.; Bernasconi, C.; Shynkarenko, Y.; Krieg, F.; Widmer, R.; Aeschlimann, B.; Günther, D.; Kovalenko, M. V.; Infante, I. Rationalizing and Controlling the Surface Structure and Electronic Passivation of Cesium Lead Halide

Nanocrystals. *ACS Energy Lett.* **2019**, *4* (1), 63–74. https://doi.org/10.1021/acsenergylett.8b01669.

(24) Park, Y.-S.; Guo, S.; Makarov, N. S.; Klimov, V. I. Room Temperature Single-Photon Emission from Individual Perovskite Quantum Dots. *ACS Nano* **2015**, *9* (10), 10386–10393. https://doi.org/10.1021/acsnano.5b04584.

(25) Dirin, D. N.; Protesescu, L.; Trummer, D.; Kochetygov, I. V.; Yakunin, S.; Krumeich, F.; Stadie, N. P.; Kovalenko, M. V. Harnessing Defect-Tolerance at the Nanoscale: Highly Luminescent Lead Halide Perovskite Nanocrystals in Mesoporous Silica Matrixes. *Nano Lett.* **2016**, *16* (9), 5866–5874. https://doi.org/10.1021/acs.nanolett.6b02688.

(26) Houtepen, A. J.; Hens, Z.; Owen, J. S.; Infante, I. On the Origin of Surface Traps in Colloidal II–VI Semiconductor Nanocrystals. *Chem. Mater.* **2017**, *29* (2), 752–761. https://doi.org/10.1021/acs.chemmater.6b04648.

(27) Giansante, C.; Infante, I. Surface Traps in Colloidal Quantum Dots: A Combined Experimental and Theoretical Perspective. *J. Phys. Chem. Lett.* **2017**, *8* (20), 5209–5215. https://doi.org/10.1021/acs.jpclett.7b02193.

(28) Fausia, K. H.; Nharangatt, B.; Vinayakan, R. N.; Ramesh, A. R.; Santhi, V.; Dhandapani, K. R.; Manoj, T. P.; Chatanathodi, R.; Jose, D.; Sandeep, K. Probing the Structural Degradation of $CsPbBr_3$ Perovskite Nanocrystals in the Presence of H_2 O and H_2 S: How Weak Interactions and HSAB Matter. *ACS Omega* **2024**, acsomega.3c09600. https://doi.org/10.1021/acsomega.3c09600.

(29) Hidalgo, J.; Kaiser, W.; An, Y.; Li, R.; Oh, Z.; Castro-Méndez, A.-F.; LaFollette, D. K.; Kim, S.; Lai, B.; Breternitz, J.; Schorr, S.; Perini, C. A. R.; Mosconi, E.; De Angelis, F.; Correa-Baena, J.-P. Synergistic Role of Water and Oxygen Leads to Degradation in

Formamidinium-Based Halide Perovskites. *J. Am. Chem. Soc.* **2023**, jacs.3c05657. https://doi.org/10.1021/jacs.3c05657.

(30) Fiuza-Maneiro, N.; Sun, K.; López-Fernández, I.; Gómez-Graña, S.; Müller-Buschbaum, P.; Polavarapu, L. Ligand Chemistry of Inorganic Lead Halide Perovskite Nanocrystals. *ACS Energy Lett.* **2023**, *8* (2), 1152–1191. https://doi.org/10.1021/acsenergylett.2c02363.

(31) De Roo, J.; Ibáñez, M.; Geiregat, P.; Nedelcu, G.; Walravens, W.; Maes, J.; Martins, J. C.; Van Driessche, I.; Kovalenko, M. V.; Hens, Z. Highly Dynamic Ligand Binding and Light Absorption Coefficient of Cesium Lead Bromide Perovskite Nanocrystals. *ACS Nano* **2016**, *10* (2), 2071–2081. https://doi.org/10.1021/acsnano.5b06295.

(32) Milanese, S.; De Giorgi, M. L.; Morello, G.; Bodnarchuk, M. I.; Anni, M. Role of the Capping Ligand in $CsPbBr_3$ Nanocrystals Amplified Spontaneous Emission Properties. *ACS Appl. Nano Mater.* **2025**, *8* (8), 3964–3973. https://doi.org/10.1021/acsanm.4c06792.

(33) Krieg, F.; Ong, Q. K.; Burian, M.; Rainò, G.; Naumenko, D.; Amenitsch, H.; Süess, A.; Grotevent, M. J.; Krumeich, F.; Bodnarchuk, M. I.; Shorubalko, I.; Stellacci, F.; Kovalenko, M. V. Stable Ultraconcentrated and Ultradilute Colloids of $CsPbX_3$ (X = Cl, Br) Nanocrystals Using Natural Lecithin as a Capping Ligand. *J. Am. Chem. Soc.* **2019**, *141* (50), 19839–19849. https://doi.org/10.1021/jacs.9b09969.

(34) Hofmann, A.; Schmid, M.; Brütting, W. The Many Facets of Molecular Orientation in Organic Optoelectronics. *Adv. Opt. Mater.* **2021**, *9* (21), 2101004. https://doi.org/10.1002/adom.202101004.

(35) Russ, B.; Lin, T.-T.; Elenteny, H.; Eisler, C. N. Quantifying the Accuracy and Precision of the Transition Dipole Moment Alignment from Realistic Angular Emission Data. *ACS Photonics* **2025**, *12* (6), 3217–3226. https://doi.org/10.1021/acsphotonics.5c00684.

(36) Hofmann, A.; Schmid, M.; Brütting, W. The Many Facets of Molecular Orientation in Organic Optoelectronics. *Adv. Opt. Mater.* **2021**, *9* (21), 2101004. https://doi.org/10.1002/adom.202101004.

(37) Schmidt, T. D.; Lampe, T.; Sylvinson M. R., D.; Djurovich, P. I.; Thompson, M. E.; Brütting, W. Emitter Orientation as a Key Parameter in Organic Light-Emitting Diodes. *Phys. Rev. Appl.* **2017**, *8* (3), 037001. https://doi.org/10.1103/PhysRevApplied.8.037001.

(38) Araújo, G. L.; Martí, A. Absolute Limiting Efficiencies for Photovoltaic Energy Conversion. *Sol. Energy Mater. Sol. Cells* **1994**, *33* (2), 213–240. https://doi.org/10.1016/0927-0248(94)90209-7.

(39) Saxena, K.; Jain, V. K.; Mehta, D. S. A Review on the Light Extraction Techniques in Organic Electroluminescent Devices. *Opt. Mater.* **2009**, *32* (1), 221–233. https://doi.org/10.1016/j.optmat.2009.07.014.

(40) Kim, K.; Kim, J. Origin and Control of Orientation of Phosphorescent and TADF Dyes for High-Efficiency OLEDs. *Adv. Mater.* **2018**, *30* (42), 1705600. https://doi.org/10.1002/adma.201705600.

(41) Colvin, V. L.; Alivisatos, A. P. CdSe Nanocrystals with a Dipole Moment in the First Excited State. *J. Chem. Phys.* **1992**, *97* (1), 730–733. https://doi.org/10.1063/1.463573.

(42) Gao, Y.; Weidman, M. C.; Tisdale, W. A. CdSe Nanoplatelet Films with Controlled Orientation of Their Transition Dipole Moment. *Nano Lett.* **2017**, *17* (6), 3837–3843. https://doi.org/10.1021/acs.nanolett.7b01237.

(43) Jurow, M. J.; Lampe, T.; Penzo, E.; Kang, J.; Koc, M. A.; Zechel, T.; Nett, Z.; Brady, M.; Wang, L.-W.; Alivisatos, A. P.; Cabrini, S.; Brütting, W.; Liu, Y. Tunable Anisotropic

Photon Emission from Self-Organized CsPbBr3 Perovskite Nanocrystals. *Nano Lett.* **2017**, *17* (7), 4534–4540. https://doi.org/10.1021/acs.nanolett.7b02147.

(44) Jurow, M. J.; Morgenstern, T.; Eisler, C.; Kang, J.; Penzo, E.; Do, M.; Engelmayer, M.; Osowiecki, W. T.; Bekenstein, Y.; Tassone, C.; Wang, L.-W.; Alivisatos, A. P.; Brütting, W.; Liu, Y. Manipulating the Transition Dipole Moment of $CsPbBr_3$ Perovskite Nanocrystals for Superior Optical Properties. *Nano Lett.* **2019**, *19* (4), 2489–2496. https://doi.org/10.1021/acs.nanolett.9b00122.

(45) Parsons, L. E.; Russ, B.; Eisler, C. N. Tunable Angular Light Emission of Lead Halide Perovskite Nanocrystal Thin Films via Solution-Processed Substrate Treatment. *ACS Nanosci. Au* **2025**, *5* (4), 276–283. https://doi.org/10.1021/acsnanoscienceau.5c00054.

(46) Rainò, G.; Becker, M. A.; Bodnarchuk, M. I.; Mahrt, R. F.; Kovalenko, M. V.; Stöferle, T. Superfluorescence from Lead Halide Perovskite Quantum Dot Superlattices. *Nature* **2018**, *563* (7733), 671–675. https://doi.org/10.1038/s41586-018-0683-0.

(47) Dong, A.; Chen, J.; Vora, P. M.; Kikkawa, J. M.; Murray, C. B. Binary Nanocrystal Superlattice Membranes Self-Assembled at the Liquid–Air Interface. *Nature* **2010**, *466* (7305), 474–477. https://doi.org/10.1038/nature09188.

(48) Abbas, A. S.; Chabeda, D.; Weinberg, D.; Limmer, D. T.; Rabani, E.; Paul Alivisatos, A. Non-Monotonic Size-Dependent Exciton Radiative Lifetime in CsPbBr3 Nanocrystals. *Nat. Commun.* **2025**, *16* (1), 6401. https://doi.org/10.1038/s41467-025-60848-5.

(49) Lieb, M. A.; Zavislan, J. M.; Novotny, L. Single-Molecule Orientations Determined by Direct Emission Pattern Imaging. *J. Opt. Soc. Am. B* **2004**, *21* (6), 1210. https://doi.org/10.1364/JOSAB.21.001210.

(50) Schuller, J. A.; Karaveli, S.; Schiros, T.; He, K.; Yang, S.; Kymissis, I.; Shan, J.; Zia, R. Orientation of Luminescent Excitons in Layered Nanomaterials. *Nat. Nanotechnol.* **2013**, *8* (4), 271–276. https://doi.org/10.1038/nnano.2013.20.

(51) Kurvits, J. A.; Jiang, M.; Zia, R. Comparative Analysis of Imaging Configurations and Objectives for Fourier Microscopy. *J. Opt. Soc. Am. A* **2015**, *32* (11), 2082. https://doi.org/10.1364/JOSAA.32.002082.

(52) Krieg, F.; Sercel, P. C.; Burian, M.; Andrusiv, H.; Bodnarchuk, M. I.; Stöferle, T.; Mahrt, R. F.; Naumenko, D.; Amenitsch, H.; Rainò, G.; Kovalenko, M. V. Monodisperse Long-Chain Sulfobetaine-Capped $CsPbBr_3$ Nanocrystals and Their Superfluorescent Assemblies. *ACS Cent. Sci.* **2021**, *7* (1), 135–144. https://doi.org/10.1021/acscentsci.0c01153.

(53) Chaudhary, B.; Kshetri, Y. K.; Kim, H.-S.; Lee, S. W.; Kim, T.-H. Current Status on Synthesis, Properties and Applications of $CsPbX_3$ (X = Cl, Br, I) Perovskite Quantum Dots/Nanocrystals. *Nanotechnology* **2021**, *32* (50), 502007. https://doi.org/10.1088/1361-6528/ac2537.

(54) Bertolotti, F.; Nedelcu, G.; Vivani, A.; Cervellino, A.; Masciocchi, N.; Guagliardi, A.; Kovalenko, M. V. Crystal Structure, Morphology, and Surface Termination of Cyan-Emissive, Six-Monolayers-Thick $CsPbBr_3$ Nanoplatelets from X-Ray Total Scattering. *ACS Nano* **2019**, *13* (12), 14294–14307. https://doi.org/10.1021/acsnano.9b07626.

(55) Zhang, B.; Goldoni, L.; Lambruschini, C.; Moni, L.; Imran, M.; Pianetti, A.; Pinchetti, V.; Brovelli, S.; De Trizio, L.; Manna, L. Stable and Size Tunable $CsPbBr_3$ Nanocrystals Synthesized with Oleylphosphonic Acid. *Nano Lett.* **2020**, *20* (12), 8847–8853. https://doi.org/10.1021/acs.nanolett.0c03833.

(56) Ten Brinck, S.; Infante, I. Surface Termination, Morphology, and Bright Photoluminescence of Cesium Lead Halide Perovskite Nanocrystals. *ACS Energy Lett.* **2016**, *1* (6), 1266–1272. https://doi.org/10.1021/acsenergylett.6b00595.

(57) Boles, M. A.; Ling, D.; Hyeon, T.; Talapin, D. V. The Surface Science of Nanocrystals. *Nat. Mater.* **2016**, *15* (2), 141–153. https://doi.org/10.1038/nmat4526.

(58) Park, J. Y.; Chen, D.; Li, S.; Xia, Y.; Diroll, B. T.; Guo, P. Quantifying Size Effects on Thermal Transport in $CsPbBr_3$ Nanocrystal Films. *Nano Lett.* **2025**, *25* (39), 14286–14292. https://doi.org/10.1021/acs.nanolett.5c03215.

(59) Sun, S.; Huang, P.; Wu, X.; Chen, C.; Hu, X.; Bai, Z.; Pushkarev, A.; Zhong, H. Ligand Exchange-Induced Shape Transformation of $CsPbBr_3$ Nanocrystals Boosts the Efficiency of Perovskite Light-Emitting Diodes. *J. Phys. Chem. C* **2024**, *128* (8), 3602–3608. https://doi.org/10.1021/acs.jpcc.4c00155.

(60) Jurow, M. J.; Lampe, T.; Penzo, E.; Kang, J.; Koc, M. A.; Zechel, T.; Nett, Z.; Brady, M.; Wang, L.-W.; Alivisatos, A. P.; Cabrini, S.; Brütting, W.; Liu, Y. Tunable Anisotropic Photon Emission from Self-Organized $CsPbBr_3$ Perovskite Nanocrystals. *Nano Lett.* **2017**, *17* (7), 4534–4540. https://doi.org/10.1021/acs.nanolett.7b02147.

(61) Miranti, R.; Komatsu, R.; Enomoto, K.; Inoue, D.; Pu, Y.-J. Symmetry-Broken Electronic State of $CsPbBr_3$ Cubic Perovskite Nanocrystals. *J. Phys. Chem. Lett.* **2024**, *15* (39), 10009–10017. https://doi.org/10.1021/acs.jpclett.4c02160.

(62) Shcherbakov-Wu, W.; Saris, S.; Sheehan, T. J.; Wong, N. N.; Powers, E. R.; Krieg, F.; Kovalenko, M. V.; Willard, A. P.; Tisdale, W. A. Persistent Enhancement of Exciton Diffusivity in $CsPbBr_3$ Nanocrystal Solids. *Sci. Adv.* **2024**, *10* (8), eadj2630. https://doi.org/10.1126/sciadv.adj2630.

(63) Singh, J.; Whitten, J. E. Adsorption of 3-Mercaptopropyltrimethoxysilane on Silicon Oxide Surfaces and Adsorbate Interaction with Thermally Deposited Gold. *J. Phys. Chem. C* **2008**, *112* (48), 19088–19096. https://doi.org/10.1021/jp807536z.

(64) Pietra, F.; Rabouw, F. T.; Evers, W. H.; Byelov, D. V.; Petukhov, A. V.; De Mello Donegá, C.; Vanmaekelbergh, D. Semiconductor Nanorod Self-Assembly at the Liquid/Air Interface Studied by in Situ GISAXS and Ex Situ TEM. *Nano Lett.* **2012**, *12* (11), 5515–5523. https://doi.org/10.1021/nl302360u.

(65) Diroll, B. T.; Greybush, N. J.; Kagan, C. R.; Murray, C. B. Smectic Nanorod Superlattices Assembled on Liquid Subphases: Structure, Orientation, Defects, and Optical Polarization. *Chem. Mater.* **2015**, *27* (8), 2998–3008. https://doi.org/10.1021/acs.chemmater.5b00355.

(66) Sekh, T. V.; Cherniukh, I.; Kobiyama, E.; Sheehan, T. J.; Manoli, A.; Zhu, C.; Athanasiou, M.; Sergides, M.; Ortikova, O.; Rossell, M. D.; Bertolotti, F.; Guagliardi, A.; Masciocchi, N.; Erni, R.; Othonos, A.; Itskos, G.; Tisdale, W. A.; Stöferle, T.; Rainò, G.; Bodnarchuk, M. I.; Kovalenko, M. V. All-Perovskite Multicomponent Nanocrystal Superlattices. *ACS Nano* **2024**, *18* (11), 8423–8436. https://doi.org/10.1021/acsnano.3c13062.

(67) Parsons, L. E.; Grishchenko, A. Y.; Eisler, C. N. Oriented Dipoles in Ordered Ensembles of Confined Lead Halide Perovskite Nanocrystals. *J. Phys. Chem. C* **2026**, acs.jpcc.5c07457. https://doi.org/10.1021/acs.jpcc.5c07457.

(68) Kambhampati, P. Learning about the Structural Dynamics of Semiconductor Perovskites from Electron Solvation Dynamics. *J. Phys. Chem. C* **2021**, *125* (43), 23571–23586. https://doi.org/10.1021/acs.jpcc.1c07445.

(69) Liu, F.; Sidhik, S.; Hoffbauer, M. A.; Lewis, S.; Neukirch, A. J.; Pavlenko, V.; Tsai, H.; Nie, W.; Even, J.; Tretiak, S.; Ajayan, P. M.; Kanatzidis, M. G.; Crochet, J. J.; Moody, N.

A.; Blancon, J.-C.; Mohite, A. D. Highly Efficient Photoelectric Effect in Halide Perovskites for Regenerative Electron Sources. *Nat. Commun.* **2021**, *12* (1), 673. https://doi.org/10.1038/s41467-021-20954-6.

(70) Kurvits, J. A.; Jiang, M.; Zia, R. Comparative Analysis of Imaging Configurations and Objectives for Fourier Microscopy. *J. Opt. Soc. Am. A* **2015**, *32* (11), 2082. https://doi.org/10.1364/JOSAA.32.002082.

(71) Schuller, J. A.; Karaveli, S.; Schiros, T.; He, K.; Yang, S.; Kymissis, I.; Shan, J.; Zia, R. Orientation of Luminescent Excitons in Layered Nanomaterials. *Nat. Nanotechnol.* **2013**, *8* (4), 271–276. https://doi.org/10.1038/nnano.2013.20.

(72) Gao, Y.; Weidman, M. C.; Tisdale, W. A. CdSe Nanoplatelet Films with Controlled Orientation of Their Transition Dipole Moment. *Nano Lett.* **2017**, *17* (6), 3837–3843. https://doi.org/10.1021/acs.nanolett.7b01237.

(73) Bekenstein, Y.; Koscher, B. A.; Eaton, S. W.; Yang, P.; Alivisatos, A. P. Highly Luminescent Colloidal Nanoplates of Perovskite Cesium Lead Halide and Their Oriented Assemblies. *J. Am. Chem. Soc.* **2015**, *137* (51), 16008–16011. https://doi.org/10.1021/jacs.5b11199.